Active tectonic field for CO_2 Storage management: Hontomín onshore study-case (SPAIN)

Raúl Pérez-López[1], José F. Mediato[1], Miguel A. Rodríguez-Pascua[1], Jorge L. Giner-Robles[2], Adrià Ramos[1], Silvia Martín-Velázquez[3], Roberto Martínez-Orío[1], Paula Fernández-Canteli[1]

1. IGME – Instituto Geológico y Minero de España – Geological Survey of Spain. C/Ríos Rosas 23, Madrid 28003 – SPAIN. Email: r.perez@igme.es, jf.mediato@igme.es, ma.rodriguez@igme.es, a.ramos@igme.es, ro.martinez@igme.es, paula.canteli@igme.es
2. Departamento de Geología y Geoquímica. Facultad de Ciencias. Universidad Autónoma de Madrid. Campus Cantoblanco, Madrid. SPAIN. Email: jorge.giner@uam.es
3. Universidad Rey Juan Carlos. Email: silvia.martin@urjc.es

Abstract

One of the concerns of underground CO_2 onshore storage is the triggering of Induced Seismicity and fault reactivation by pore pressure increasing. Hence, a comprehensive analysis of the tectonic parameters involved in the storage rock formation is mandatory for safety management operations. Unquestionably, active faults and seal faults depicting the storage bulk are relevant parameters to be considered. However, there is a lack of analysis of the active tectonic strain field affecting these faults during the CO_2 storage monitoring. The advantage of reconstructing the tectonic field is the possibility to determine the strain trajectories and describing the fault patterns affecting the reservoir rock. In this work, we adapt a methodology of systematic geostructural analysis to the underground CO_2 storage, based on the calculation of the strain field and defined by the strain field from kinematics indicators on the fault planes (e_y and e_x for the maximum and minimum horizontal shortening respectively). This methodology is based on a statistical analysis of individual strain tensor solutions obtained from fresh outcrops from Triassic to Miocene. Consequently, we have collected 447 fault data in 32 field stations located within a 20 km radius. The understanding of the fault sets role for underground fluid circulation can also be established, helping for further analysis of CO_2 leakage and seepage. We have applied this methodology to Hontomín onshore CO_2

storage facilities (Central Spain). The geology of the area and the number of high-quality outcrops made this site as a good candidate for studying the strain field from kinematics fault analysis. The results indicate a strike-slip tectonic regime with the maximum horizontal shortening with N160°E and N50ºE trend for the local regime, which activates NE-SW strike-slip faults. A regional extensional tectonic field was also recognized with N-S trend, which activates N-S extensional faults, and NNE-SSW and NNW-SSE strike-slip faults, measured in the Cretaceous limestone on top of the Hotomín facilities. Monitoring these faults within the reservoir is suggested in addition to the possibility of obtaining focal mechanism solutions for microearthquakes (M < 3).

Keywords: onshore CO_2 storage, tectonic field, paleostrain analysis, active fault, Hontomín onshore pilot-plant.

1. INTRODUCTION

Industrial made-man activities generate CO_2 that could change the chemical balance of the atmosphere and their relationship with the geosphere. The Geological Carbon Storage (GSC) appears as a good choice to reduce the CO_2 gas emission to the atmosphere (Christensen, 2004), allowing the industry increasing activity with a low pollution impact. There is a lot of literature about what must have a site to be a potential underground storage suitable to GSC (e.g. Chu, 2009; Orr, 2009; Goldberg et al., 2010 among others). The reservoir sealing, the caprock, permeability and porosity, plus injection pressure and volume injected, are the main considerations to choose one geological subsurface formation as the CO_2 host-rock. In this frame, the tectonic active field is considered in two principal ways: (1) to prevent the fault activation and earthquakes triggering, with the consequence of leakage and seepage, and (2) the long-term reservoir behavior, understanding as long-term from centennial to millennial time-span. Therefore, what is the long-term behavior of GSC? What do we need to monitor for a safe GSC management? Winthaegen et al. (2005) suggest three subjects for monitoring: (a) the atmosphere air quality near the injection facilities, due to the CO_2 toxicity (values greater than 4%, see Rice, 2003 and Permentier et al., 2017), (b) the overburden monitoring faults and wells and (c) the sealing of the reservoir. The study of natural analogues for GSC is a good strategy to estimate the long-term behavior of the reservoir, considering parameters as the injected CO_2 pressure and volume, plus the brine mixing with CO_2 (Pearce, 2006). Hence, the prediction of site performance over long timescales also requires an understanding of CO_2 behavior within the reservoir, the mechanisms of migration out of the reservoir, and the potential impacts of a leak on the near surface environment. The assessments of such risks will rely on a combination of predictive models of CO_2 behavior, including the fluid migration and the long-term CO_2-porewater-mineralogical interactions (Pearce, 2006). Once again, the tectonic active field interacts directly on this assessment. Moreover, the fault reactivation due to the pore pressure increasing during the injection and storage has also to be considered (Röhmann et al., 2013). Despite the uplift measure by Röhmann et al. (2013) are submillimeter (c.a. 0.021 mm) at the end of the injection processes, given the ongoing occurrence of microearthquakes, long-term monitoring is required. The geomechanical and geological models predict the reservoir behavior and the caprock sealing properties. The role of the faults inside these models is crucial for the tectonic long-term behavior and the reactivation of faults that could trigger earthquakes.

Concerning the Induced Seismicity, Wilson et al. (2017) published the Hi-Quake database, with a classification of all man-made earthquakes according to the literature, in an online repository (https://inducedearthquakes.org/, last access on May, 2019). This database includes 834 projects with proved Induced Seismicity, where two different cases with earthquakes as large as M 1.7, detected in swarms about 9,500 microearthquakes, are related to GSC operations. Additionally, Foulger et al. (2018) pointed out that GSC can trigger earthquakes with magnitudes lesser than M 2, namely the cases described in their work are as great as M 1.8, with the epicenter location 2 km around the facilities. McNamara (2016) described a comprehensive method and protocol for monitoring GSC reservoir for the assessment and management of Induced Seismicity. The knowledge of active fault patterns and the stress/strain field could help on designing monitoring network and identifying those faults capable of triggering micro-earthquakes (M < 2) and/or breaking the sealing for leakage (patterns of open faults for low-permeability CO_2 migration).

In this work, we propose that the description, the analysis and establishment of the tectonic strain field have to be mandatory for long-term GSC monitoring and management, implementing the fault behavior in the geomechanical models. This analysis does not increase the cost for long-term monitoring, given that they are low-cost and the results are acquired in a few months. Therefore, we propose a methodology based on the reconstruction of the strain field from the classical studies in geodynamics (Angelier, 1979 and 1984; Reches, 1983; Reches, 1987). As a novelty, we introduce the strain fields (SF) analysis between 20 away from the subsurface reservoir deep geometry, under the area of influence of induced seismicity for fluid injection. The knowledge of the strain field at local scale allows classifying the type of faulting and their role for leakage processes, whilst the regional scale explores the tectonic active faults that could affect the reservoir. The methodology is rather simple, taking measures of slickensides and striations on fault planes to establish the orientation of the maximum horizontal shortening (e_y), and the minimum horizontal shortening (e_x) for the strain tensor. The principal advantage of the SF analysis is the directly classification of all the faults involved into the geomechanical model and the prediction of the failure parameters. Besides, a Mohr-Coulomb failure analysis was performed to the fault pattern recognized in the Cretaceous outcrop located on top of the pilot plant.

The tectonic characterization of the GSC of Hontomín was implemented in the geological model described by Le Gallo and de Dios (2018). Beyond the use of Induced Seismicity and potentially active faults, the scope of this method is to propose an initial analysis to manage underground storage operations. We present how the Structural Analysis of fault/slip data can improve the knowledge of the tectonic large-scale fault network for the potential seismic reactivation during fluid injection and time-depend scale for fluid stays.

2. HONTOMÍN ONSHORE STUDY CASE

2.1 Geological description of the reservoir

The CO_2 storage site of Hontomín is enclosed in the southern section of the Mesozoic Basque–Cantabrian Basin, known as Burgalesa Platform (Serrano and Martinez del Olmo, 1990; Tavani, 2012), within the sedimentary Bureba Basin (**Fig. 1**). This geological domain is located in the northern junction of the Cenozoic Duero and Ebro basins, forming an ESE-dipping monocline bounded by the Cantabrian Mountains Thrust to the north, the Ubierna Fault System (UFS) to the south and the Asturian Massif to the west (**Fig. 1**).

The Meso-Cenozoic tectonic evolution of the Burgalesa Platform starts with a first rift period during Permian and Triassic times (Dallmeyer and Martínez-García, 1990; Calvet et al., 2004), followed by a relative tectonic quiescence during Early and Middle Jurassic times (e.g. Aurell et al., 2002). The main rifting phase took place during the

Late Jurassic and Early Cretaceous times, due to the opening of the North Atlantic and the Bay of Biscay-Pyrenean rift system (García-Mondéjar et al., 1986; Le Pichon and Sibuet, 1971; Lepvrier and Martínez-García, 1990; García-Mondéjar et al., 1996; Roca et al., 2011; Tugend et al., 2014). The convergence between Iberia and Eurasia from Late Cretaceous to Miocene times triggered the inversion of previous Mesozoic extensional faults and the development of an E-W orogenic belt (Cantabrian domain to the west and Pyrenean domain to the east) formed along the northern Iberian plate margin (Muñoz, 1992; Gómez et al., 2002; Vergés et al., 2002).

The Hontomín facilities are located within the Basque-Cantabrian Basin (**Fig. 1b**). The geological reservoir structure is bordered by the UFS to the south and west, by the Poza de la Sal diapir and the Zamanzas Popup structure (Carola, 2014) to the north and by the Ebro Basin to the east (**Fig. 1**). The structure is defined as a forced fold related dome structure (Tavani et al., 2013; **Fig. 2**), formed by an extensional fault system with migration of evaporites towards the hanging wall during the Mesozoic (Soto et al., 2011). During the tectonic compressional phase, associated with the Alpine Orogeny affecting the Pyrenees, the right-lateral transpressive inversion of the basement faults was activated, along with the reactivation of transverse extensional faults (**Fig. 2**; Tavani et al., 2013; Alcalde et al., 2014).

The target reservoir and seal formations consist of Lower Jurassic marine carbonates, arranged in an asymmetric dome-like structure (**Fig. 2**) with an overall extent of 15 km^2 and located at 1,485 m of depth (Alcalde et al., 2013, 2014; Ogaya et al., 2013). The target CO_2 injection point is a saline aquifer formed by a dolostone unit, known as "Carniolas", and an oolitic limestone of the Sopeña Formation, both corresponding to Lias in time (Early Jurassic). The estimated porosity of the Carniolas reaches over 12% (Ogaya et al., 2013; Le Gallo and de Dios, 2018) and it is slightly lower at the

Carbonate Lias level (8.5% in average). The reservoir levels contain saline water with more than 20 g/l of NaCl and very low oil content. The high porosity of the lower part of the reservoir (i.e., the Carniolas level) is the result of secondary dolomitization and different fracturing events (Alcalde et al., 2014). The minimum thickness of the reservoir units is 100 m. The potential upper seal unit comprises Lias marlstones and black shales from a hemipelagic ramp (**Fig. 2**); Pliensbachian and Toarcian) of the "Puerto del Pozazal" and Sopeña Formations.

2.2 Regional tectonic field

The tectonic context has been described from two different approaches: (1) the tectonic style of the fractures bordering the Hontomín reservoir (De Vicente et al., 2011; Tavani et al., 2011) and (2) the tectonic regional field described from earthquakes with mechanism solutions and GPS data (Herraiz et al., 2000; Stich et al., 2006; De Vicente et al., 2008).

(1) The tectonic style of the Bureba Basin was described by De Vicente et al. (2011), which classified the Basque-Cantabrian Cenozoic Basin (**Fig. 1a**) as transpressional with contractional horsetail splay basin. The NW-SE oriented Ventaniella fault (**Fig. 1a**), includes the UFS in the southeastward area, being active between the Permian and Triassic period, and strike-slip during the Cenozoic contraction. In this tectonic configuration, the Ubierna Fault acts as a right-lateral strike-slip fault. These authors pointed out the sharp contacts between the thrusts and the strike-slip faults in this basin. Furthermore, Tavani et al. (2011) also described complex Cenozoic tectonic context where right-lateral tectonic style reactivated WNW-ESE trending faults. Both the Ventaniella and the Ubierna faults acted as transpressive structures forming 120 km long and 15 km wide of the UFS, and featured by 0.44 mm/yr of averaged tectonic

strike-slip deformation between the Oligocene and the present day. The aforementioned authors described different surface segments of the UFS of right-lateral strike-slip ranging between 12 and 14 km length. The structural data collected by Tavani et al. (2011) pointed out the 60% of data correspond to right lateral strike-slip with WNW-ESE trend, together with conjugate reverse faulting with NE-SW, NW-SE and E-W trend, and left-lateral strike-slip faults N-S oriented. They concluded that this scheme could be related to a transpressional right-lateral tectonic system with a maximum horizontal compression, S_{Hmax}, striking N120ºE. Concerning the geological evidence of recent sediments affected by tectonic movements of the UFS, Tavani et al. (2011) suggest Middle Miocene in time for this tectonic activity. However, geomorphic markets (river and valley geomorphology) could indicate tectonic activity at present-times. All of these data correspond to regional or small-scale data collected to explain the Basque-Cantabrian Cenozoic transpressive basin. The advantage of the methodology proposed here to establish the tectonic local regime affecting the reservoir, is the searching for local-scale tectonics (20 km sized), and the estimation of the depth for the non-deformation surface for strata folding in transpressional tectonics (Lisle et al., 2009).

(2) Regarding the stress field from earthquake focal mechanism solutions, Herraiz et al. (2000) pointed out the regional trajectories of S_{Hmax} with NNE-SSW trend, and with a NE-SW S_{Hmax} trend from slip-fault inversion data. Stich et al. (2006) obtained the stress field from seismic moment tensor inversion and GPS data. These authors pointed out a NW-SE Africa-Eurasia tectonic convergence at tectonic rate of 5 mm/yr approximately. However, no focal mechanism solutions are found within the Hontomín area (20 km) and only long-range spatial correlation could be made with high uncertainty (in time, space and magnitude). The same lack of information appears in the work of De Vicente

et al. (2008), with no focal mechanism solutions in the 50 km surrounding the HPP. In this work, these authors classified the tectonic regime as uniaxial extension to strike-slip with NW-SE S_{Hmax} trend.

Regional data about the tectonic field inferred from different works (Herraiz et al., 2000; Stich et al., 2006; De Vicente et al., 2008, 2011; Tavani et al., 2011; Tavani, 2012), show differences for the S_{Hmax}. These works explain the tectonic framework for regional scale. Nevertheless, local tectonics could determine the low permeability and the potential induced seismicity within the reservoir. In the next section, we have applied the methodology described at the section 3 of this manuscript, in order to compare the regional results from these works and to establish the tectonic evolution of the Burgalesa Platform.

2.3 Strategy of the ENOS European Project

Hontomín pilot-plant (HPP) for CO_2 onshore storage is the only one in Europe recognized as a key-test-facility, and it is managed and conducted by CIUDEN (*Fundación Ciudad de la Energía*). The HPP is located within the province of Burgos (**Fig. 1b**), in the northern central part of Spain.

The methodology proposed in this work and its application for long-term onshore GSC managing in the frame of geological risk, is based on the strain tensor calculation, as part of the objectives proposed in the European project “ENabling Onshore CO2 Storage in Europe” (ENOS). The ENOS project is an initiative of CO2GeoNet, the European Network of Excellence on the geological storage of CO_2 for supporting onshore storage and fronting the associated troubles as GSC perception, the safe storage operation, potential leaking management and health, and environmental safety (Gastine et al., 2017). ENOS combines a multidisciplinary European project, which focuses in onshore storage, with the demonstration of best practices through pilot-scale projects in the case of Hontomín facilities. Moreover, this project claims for creating a favorable environment for GSC onshore through public engagement, knowledge sharing, and training (Gastine et al., 2017). In this context, the work-package WP1 is devoted to “ensuring safe storage operations”.

3. METHODS AND RATIONALE

The lithosphere remains in a permanent state of deformation, related to plate tectonics motion. Strain and stress fields are the consequence of this deformation on the upper lithosphere, arranging different fault patterns that determine sedimentary basins and geological formations. Kinematics of these faults describes the stress/strain fields, for example measuring grooves and slickensides on fault planes (see Angelier, 1979, Reches, 1983 among others). The relevance of the tectonic field is that stress and strain determine the earthquake occurrence by the fault activity. In this work, we have performed a brittle analysis of the fault kinematics, by measuring slickenfiber on fault planes (dip/ dip direction and rake), in several outcrops in the surroundings of the onshore reservoir. To carry out the methodology proposed in this work, the study area was divided in a circle with four equal areas, and we searched outcrops of fresh rock to perform the fault kinematic analysis. This allows establishing a realistic tectonic very-near field to be considered during the storage seismic monitoring and long-term management. Finally, we have studied the fault plane reactivation by using the Mohr-Coulomb failure criterion (Pan et al., 2016), from the fault pattern obtained in the Cretaceous limestone outcrop located on top of the HPP facilities.

3.1 *Paleostrain Analysis*

We have applied the strain inversion technique to reconstruct the tectonic field (paleostrain evolution), affecting the Hontomín site between the Triassic, Jurassic, Cretaceous and Neogene ages (late Miocene to present times). For a further methodology explanation, see Etchecopar et al. (1981), Reches (1983) and Angelier (1990). The main assumption for the inversion technique of fault population is the self-similarity to the scale invariance for the stress/strain tensors. This means that we can calculate the whole stress/strain fields by using the slip data on fault planes and for homogeneous tectonic frameworks. The strain tensor is an ellipsoid defined by the orientation of the three principal axes and the shape of the ellipsoid (k). This method assumes that the slip-vectors, obtained from the pitch of the striation on different fault planes, define a common strain tensor or a set in a homogeneous tectonic arrangement. We assume that the strain field is homogeneous in space and time, the number of faults activated is greater than five and the slip vector is parallel to the maximum shear stress (τ).

The inversion technique is based on the Bott equations (Bott, 1959). These equations show the relationship between the orientation and the shape of the stress ellipsoid:

$$\mathrm{Tan}\,(\theta) = [n / (l * m)] * [m^2 - (1- n^2) * R'] \qquad \text{[eq.1]}$$

$$R' = (\sigma_z - \sigma_x) / (\sigma_y - \sigma_x) \qquad \text{[eq.2]}$$

Where l, m and n are the direction cosines of the normal to the fault plane, θ is the pitch of the striation and R’ is the shape of the stress ellipsoid obtained in an orthonormal coordinate system, x, y, z. In this system, σ_y is the maximum horizontal stress, σ_x is the minimum horizontal stress axis and σ_z is the vertical stress axis.

3.2 The Right-Dihedral Model for Paleostrain Analysis

The Right-Dihedral (RD) is a semi-quantitative method based on the overlapping of compressional and extensional zones by using a stereographic plot. The final plot is an interferogram figure, which usually defines the strain-regime. This method is strongly robust for conjugate fault sets and with different dip values for a same tensor. The RD was originally defined by Pegoraro (1972) and Angelier and Mechler (1977), as a geometric method, adjusting the measured fault-slip data (slickensides) in agreement with theoretical models for extension and compressive fault-slip. Therefore, we can constraint the regions of maximum compression and extension related to the strain regime.

3.3 The Slip Model for the Paleostrain Analysis

The Slip Model (SM) is based on the Navier-Coulomb fracturing criteria (Reches, 1983), taking the Anderson model solution for this study (Anderson, 1951; Simpson, 1997). The Anderson model represents the geometry of the fault plane as monoclinic, relating the quantitative parameters of the shape parameter (K') with the internal frictional angle for rock mechanics (ϕ) (De Vicente 1988; Capote et al., 1991). Moreover, this model is valid for neoformed faults, and some considerations have to be accounted for previous faults and weakness planes present in the rock. These considerations are related to the dip of normal and compressional faults, such as for compressional faulting dip values lower than 45º, reactivated as extensional faults. This model shows the relationships between the K', ϕ and the direction cosines for the striation on the fault plane (De Vicente, 1988; Capote et al., 1991):

$$K' = e_y / e_z \quad \text{[eq.3]}$$

Where e_z is the vertical strain axis, e_y is the maximum horizontal shortening and e_x is the minimum horizontal shortening. This model assumes that there is no change of volume during the deformation and $e_y = e_x + e_z$.

For isotropic solids, principal strain axes coincide with the principal stress axes. This means that in this work, the orientation of the principal stress axis, S_{Hmax} is parallel to the orientation of the principal strain axes, e_y, and hence, the minimum stress axis, S_{hmin}, is parallel to the minimum strain axis, e_x. This assumption allows us to estimate the stress trajectories (S_{Hmax} and S_{hmin}) from the e_y SM results.

Resolving the equations of Anderson for different values (Anderson, 1951), we can classify the tectonic regime that activates one fault from the measurement of the fault dip, sense of dip (0º-360º) and pitch of the slickenside, assuming that one of the principal axes (e_x, e_y or e_z) is vertical (Angelier, 1984). We can classify the tectonic regime and represent the strain tensor by using the e_y and e_x orientation.

3.4 The K' strain diagram

Another analysis can be achieved by using the K'-strain diagram developed by Kaverina et al. (1996) and codified in python-code by Álvarez-Gómez (2014). These authors have developed a triangular representation based on the fault-slip, where tectonic patterns can be discriminated between strike-slip and dip-slip types. This diagram is divided in 7 different zones according to the type of fault: (1) pure normal, (2) pure reverse and (3) pure strike-slip; combined with the possibility of oblique faults: (4) reverse strike-slip and (5) strike-slip with reverse component; and lateral faults: (6) normal strike-slip and (7) strike-slip faults with normal component (**Fig. 3**). Strike-slip faults are defined by small values for pitch ($p < 25º$), and dips close to vertical planes ($\beta > 75º$). High pitch values (p > 60º) are related to normal or/reverse fault-slip vectors. Extensional faults show e_y in vertical whereas compressional faults show e_y in horizontal plane.

This method was originally performed for earthquake focal mechanism solutions by using the focal parameters, the nodal planes (dip and strike) and rake (Kaverina et al., 1996). The triangular graph is based on the equal-areal representation of the T, N or B and P axes in spherical coordinates (T tensile, N or B neutral and P pressure axes), and the orthogonal regression between earthquake magnitudes Ms and mb for the Harvard earthquake CMT global catalogue in 1996. Álvarez-Gómez (2014) presented a code python-based for computing the Kaverina diagrams, and we have modified the input parameters by including the K' intervals for the strain field from the SM. The relationship between the original diagram of Kaverina (**Fig. 3a**) and the K'-dip diagram (**Fig. 3b**) that we have used in this work is shown in the figure 3. The advantage of this diagram is the fast assignation of the type of fault and the tectonic regime that determine this fault pattern, and the strain axes relationship.

Table 1 summarizes the different tectonic regimes of the figure 3b showing the relationship with the strain main axes e_y, e_x and e_z. This diagram exhibits a great advantage to classify the type of fault according to the strain tensor. Therefore, we can assume the type of fault from the fault orientation affecting geological deposits for each strain tensor obtained.

3.5 The Circular-Quadrant-Search (CQS) strategy for the paleostrain analysis

In this work, we propose a low-cost strategy based on a well-known methodology for determining the stress/strain tensor affecting a GSC reservoir, which will allow the long-term monitoring of the geological and seismic behavior (**Fig. 4**). The objective is to obtain enough structural data and spatially homogeneous of faults (**Figs. 4, 5**) for reconstructing the stress/strain tensor. The key-point is the determination of the orientation of the e_y, e_x and K' to plot in a map and therefore, to establish the tectonic regime. We have chosen quadrants of the circles with the aim to obtain a high-quality spatial distribution of point for the interpretation of the local and very near strain field. Hence, data are homogeneously distributed, instead of being only concentrated in one quadrant of the circle.

Pérez-López et al. (2018) carried out a first approach to the application of this methodology at Hontomín, under the objective of the ENOS project (see next section for further details). We propose a circular searching of structural field stations (**Figs. 4, 5**), located within a 20 km radius. This circle was taken, given that active faults with the capacity of triggering earthquakes of magnitudes close to M 6, exhibits a surface rupture of tens of kilometers, according to the empirical models (Wells and Coppersmith, 1994). Moreover, Verdon et al. (2015) pointed out that the maximum distance of induced earthquakes for fluid injection is 20 km. Larger distances could not be related to the stress/strain regime within the reservoir, except for the case of large geological structures (folds, master faults, etc.). Microseismicity in GSC reservoir is mainly related to the operations during the injection/depletion stages and long-term storage (Verdon 2014; Verdon et al., 2015; McNamara, 2016).

The presence of master faults (capable to trigger earthquakes of magnitude = or > than 6 and 5 km long segment) inside the 20 km radius circle, implicates that the regional tectonic field determines the strain accumulation in kilometric fault-sized. Furthermore, the presence of master faults could increase the occurrence of micro-earthquakes, due to the presence of secondary faults prone to trigger earthquakes by their normal seismic cycle (Scholz, 2018). Bearing in mind that GSC onshore reservoirs use to be deep saline aquifers (e.g. Bentham and Kirby, 2005) as the Hontomín case (Gastine et al., 2017, Le Gallo and de Dios, 2018), which is confined in folded and fractured deep geological structures, in which local tectonics plays a key role in micro-seismicity and the possibility of CO_2 leakage.

The constraints of this strategy are related to the absence of kinematics indicators on fault planes. It could occur due to later overlapping geological processes as neoformed mineralization. Also, a low rigidness eludes the slicken fiber formation, and no kinematic data will be marked on the fault plane.. A poor spatial distribution of the outcrops was also taken into account for constraining the strategy. The age of sediments does not represent the age of the active deformations and hence, the active deformation has to be analyzed by performing alternative methods (i.e. paleoseismology, archaeoseismology).

4. RESULTS

4.1 Strain Field Analysis

We have collected 447 fault-slip data on fault planes in 32 outcrops, located within a 20 km radius circle centered at the HPP (**Fig. 5**). The age of the outcrops ranges between Early Triassic to post-Miocene and are mainly located in Cretaceous limestone and dolostone (**Fig. 5, Table 2**). However, no Jurassic outcrops were located, and only seven stations are located on Neogene sediments, ranging between Early Oligocene to Middle-Late Miocene. The small number of Neogene stations is due to the mechanical properties of the affected sediments, mainly poor-lithified marls and soft-detrital fluvial deposits. Despite that, all the Neogene stations exhibit high-quality data with a number of fault-slip data ranging between 7 and 8, enough for a minimum quality analysis.

We have labeled the outcrops with the acronym HTM followed by a number (see **figure 5** for the geographical location and **Table 2** and **figure 6** for the fault data). The station with the highest number of faults measured is HTM17 with 105 faults on Cretaceous limestone. Conjugate fault systems can be recognized in most of the stations (HTM1, 3, 5, 7, 10, 14, 16, 21, 23, 24, 25, 29, 30 and 32, **Fig. 6**), although there are a few stations with only one well defined fault set (6, 22, 32). We have to bear in mind that the recording of conjugate fault systems is more robust for the brittle analysis than recording isolated fault sets, better constraining the solution (Žaholar and Vrabec, 2008). In total, 29 of 32 stations were used (HTM24, 27, 28 with no quality data), and from these 29 stations, 21 were analyzed with the paleostrain technique. Solutions obtained here are robust to establish the paleostrain field in each outcrop as the orientation of the e_y, S_{Hmax} (**Fig. 7,**).

The results obtained from the application of the paleostrain method have been expressed in stereogram, right dihedral (RD), slip method (SM) and K'- diagram (**Fig. 7)**. The K'-diagram shows the fault classification as normal faults, normal with strike-slip component, pure strike-slip, strike-slip with reverse component and reverse faults (see **Fig. 3**). Main faults are lateral strike-slips and normal faults, followed by reverse faults, strike-slips and oblique strike-slips faults. The results of the strain regime are as follows: 1) 43% of extensional with shear component; 2) 22% of shear; 3) 13% of compressive strain (lower Cretaceous and early-middle Miocene, **Table 2**); 4)13% of pure shear and 5) 9% of shear with compression strain field, although with the presence of five reverse faults.

In contrast, we can observe that there are solutions with a double value for the e_y, S_{Hmax} orientation: HTM1, 2, 10, 11, 13, 15, 19, 26, and 30. The stations HTM3 and 23 (upper Cretaceous), show the best solution for strike-slip strain field as a pure strike-slip regime and e_y with N25°E and N99ºE trend, respectively (**Fig. 7**).

It is easy to observe the agreement between the e_y results from the SM and the K'- strain diagram, for instance, in the HTM2 the K'-diagram indicates strike-slip faults with reverse component for low dips (0º < β < 40º), but also indicates strike-slip faults with normal component for larger dips (40º < β < 90º). However, both results are in agreement with a strain field defined by the orientation for e_y, S_{Hmax} with N150º ± 18° trend. This tectonic field affects Cretaceous carbonates and coincides with the regional tectonic field proposed by Herraiz et al. (2000), Tavani et al. (2011) and Alcalde et al. (2014).

4.2 Late Triassic Outcrop Paleostrain

Strain analysis from HTM5 fault set shows e_y with NW-SE trending and shear regime with extension defined by strike-slip faults (**Figs. 7a**). This is in agreement with the uniaxial extension described in Tavani (2012), constraining this regime with S_{hmin} with NE-SW trending.

4.3 Cretaceous Outcrops Paleostrain

We have divided this result in two groups, (a) outcrops within the 20km circle from HPP and (b) the outcrop the HTM17 (**Fig. 5**), which is located in the HPP facilities and described in the next section. HTM14 is the only outcrop from Early Cretaceous age, showing a compressive tectonic stage with reverse fault solutions, defined by e_y with NE-SW trend (**Fig. 7b and 7c**). Taking into account the extensional stage related to the Main Rifting Stage that took place in Early Cretaceous times (i.e. Carola, 2004; Tavani, 2012; Tugend et al., 2014), we interpreted these results as a modern strain field, probably related to the Cenozoic Inversion stage.

Outcrops HTM 2, 3, 8, 17, 19, 20, 21, 22, 23, 25, 26, 29, 31 and 32 are from the upper Cretaceous carbonates (**Fig. 7**). Results are: (1) a compressive strain stage featured by e_y with NW-SE trend, similar to the stage described in Tavani (2012), and (2) a normal strain stage with e_y striking both E-W and NE-SW (**Fig. 7**, HTM 20, 21, 31 and 32). Finally, a (3) shear stage (activated strike-slip faults) and (4) a shear with extension (strike-slip with normal component) were described as well. These two late stages are featured by e_y with NE-SW and NW-SE trends. The existence of four different strain fields is determined by different ages during the Cretaceous and different spatial locations in relation to the main structures, the Ubierna Fault System, Hontomín Fault, Cantabrian Thrust, Montorio folded band and the Polientes syncline (**Fig. 1**).

4.4 Cretaceous Outcrop HTM17 on the Hontomín Pilot Plant

This outcrop is located on top of the geological reservoir, in a quarry of Upper Cretaceous limestones. The main advantage of this outcrop is the well-development of striation and carbonate microfibers which yields high-quality data. 105 fault-slip data were measured, with the main orientation striking N75°E; N-50ºE; and a conjugate set with N130°E (±10°) trend (**Fig. 8**). The result of the strain inversion technique shows an extensional field featured by an ey trajectory striking N107°E (±24°) related to an extensional strain field (see the K' diagram in **figure 8**). Most of the faults are extensional faults NE-SW and NW-SE oriented (**Fig. 9**), in agreement with the extensional RD solution. Reverse faults are oriented NNE-SSW, E-W and WNW-ESE. The advantage of this outcrop is the geographical and stratigraphic position. It is located on top of the HPP facilities in younger sediments than the reservoir rocks. Furthermore, given that the Jurassic reservoir rock and the Cretaceous upper unit are both composed by carbonates, the fault pattern measured here could be a reflex of the fracture network affecting the Jurassic storage rocks in depth (see **Figs. 2, 9**).

4.5 Cenozoic outcrops strain field

The Cenozoic tectonic inversion was widely described in the area by different authors (e.g. Carola, 2004; Tavani, 2012; Tungend et al., 2014). This tectonic inversion is related to compressive structures, activating NW-SE and NE-SW thrusts with NW-SE and NNE-SSW e_y trends, respectively. The Ubierna Fault has been inverted with a right-lateral transpressive kinematics during the Cenozoic (Tavani et al., 2011). Early Oligocene outcrop (HTM13, **Figs. 7c**) shows a local extensional field with e_y with NNE-SSW and N150ºE trend. During the Lower-Middle Miocene, HTM15 and HTM30 outcrops exhibit the same e_y trend, but for a compressive tectonic regime (**Figs. 7d**). HTM1 shows extensional tectonics with ey oriented N50ºE and N130ºE. Summarizing, the Cenozoic inversion and tectonic compression are detected during the Early to Middle Miocene and the Oligocene. However, during the middle Miocene only one extensional stage was interpreted (HTM1, **Fig. 7c**).

The outcrops located closer to the HPP (HTM 17, 31, 32, **Figs. 5 and 7**) show E-W faults. HTM5 is located on the Ubierna Fault, showing a NW-SE trend, whilst HTM3 shows NE-SW strike-slip.

Strain analysis suggests that the planes parallel to the S_{Hmax} orientation (NNW-SSE and N-S), could induce the leakage into the reservoir (**Fig. 7**). Moreover, N50ºE S_{Hmax} orientation could also affect the reservoir. HPP facilities are close to the Hontomin Fault (**Fig. 5**), a WNW-ESE oriented fault, although the HTM17 station shows that N-S fault planes could play an important role for seepage of fluid into the reservoir.

5. DISCUSSION

5.1 Regional active stress tensor in HTM17 fault pattern

The active regional field proposed by Herraiz et al. (2000), Stich et al. (2006), Tavani et al. (2011) and Alcalde et al. (2014), shows e_y, S_{Hmax} with almost NNW-SSE and N-S trends. Namely, the work from Herraiz et al. (2000) calculates three stress tensors within the 20 km of our study area and a Quaternary stress tensor close to the area (c.a. 40 km southward of Hontomín). The age of the first one is Miocene, and defined by σ_1 87°/331°; σ_2 01°/151°; σ_3 00°/061° (dip/dip sense 0º-360º), with an R=0.06 and S_{Hmax} trending N151ºE, under an extensional tectonic regime. Two post-Miocene stress tensors are defined by: (1) σ_1 87°/299°; σ_2 00°/209°; σ_3 01°/119° with R = 0.13, S_{Hmax} with N29°E trend under an extensional tectonic regime and (2) σ_1 00°/061°; σ_2 86°/152°; σ_3 03°/331°, with R=0.76, and S_{Hmax} N62°E under strike-slip tectonic regime. Finally, these authors calculated a Quaternary stress tensor defined by: σ_1 85°/183°; σ_2 02°/273°; σ_3 03°/003°; R=0.02 and S_{Hmax} with N101°E trend under an extensional tectonic regime. The regional active stress tensor defined for Pliocene-Quaternary ages is σ_1 88°/197°; σ_2 01°/355°; σ_3 00°/085° for 327 data with R = 0.5 and S_{Hmax} with N-S trend under an extensional tectonic regional regime.

We have applied the regional active stress tensor (Herraiz et al., 2000) for studying the reactivation of previous fault patterns measured in HTM17 (**Figs. 8** and **9**). To carry out this study, we assume that the fault plane reactivation depends on σ_1 and σ_3, and the shape of the failure envelope. Therefore, we have used the Mohr-Coulomb failure criteria for preexisting fault planes (Xu et al., 2010; Labuz and Zang, 2012), by using the Mohr Plotter v3.0 code (Allmendinger, 2012). Moreover, to calculate the Mohr-Coulomb circle, it is necessary to know the cohesion and friction parameters of the reservoir rock. Bearing in mind that the reservoir rocks are Lower-Jurassic carbonates (dolostone and oolitic limestone, Alcalde et al., 2013, 2014; Ogaya et al., 2013), we have assumed the averaged cohesion for carbonates (limestone and dolostone) in 35º and the coefficient of internal friction of 0.7 (Goodman, 1989). In addition, we have assumed no cohesion with an angle of static friction of 0.7 for preexisting faults.

Figure 10 shows the main results for the Mohr analysis. The reactivated planes under the active-present stress field are red dots, 52 out of the original 105 fault-slip measurements at HTM17. Green and orange dots indicate faults with no tectonic strength accumulation under the present-day stress field. Reactivated fault sets are oriented between N to N60ºE and N115º to 180ºE, with N-S and NNE-SSW as main trends (**Fig. 10**, red rose diagram). Under an extensional tectonic field with R = 0.5, N-S are normal faults, whereas NNE-SSW and NNW-SSE trends are strike-slips faults with extensional component. According to the results shown in figure 10, these faults could be reactivated without a pore pressure increase. The inactive fault orientation is constrained between N60ºE and N115ºE, mainly WNW-ESE (**Fig. 10**, green rose diagram). Regarding the uncertainties of these fault orientations, these values can oscillate ±5º, according to the field error measurement (averaged error for measuring structures by a compass).

Concerning the reliability of the results, some constrains need to be explained. The Mohr-Coulomb failure criterion is an approximation that assumes that the normal stress on the fault plane is not tensile. Furthermore, the increasing of pore pressure in the reservoir rock reduces the normal stress on the plane of failure and the interval of fault reactivation could be higher. This effect was not considered in the previous analysis since the calculation of the critical pore pressure is beyond the purpose of this work. Nevertheless, the MohrPlotter software (Allmendinger, 2012), allows estimating the increase of pore pressure to the critical value under some conditions.

Finally, we have applied the Slip Model and Right Dihedral to the reactivated fault-slip data from HTM17 outcrop (**Fig. 11**), by including the rake estimated from the active regional stress tensor determined by Herraiz et al. (2000). At a glance, faults oriented between N10°E and N10°W act as normal faults (4 out 52, **Figs. 11a, c**), faults between

N10°E - N50°E, and N10°W – N50°W act as extensional faults with strike-slip component (31 out 52), and NE-SW and NW-SE vertical faults act as pure strike slips (8 out 52). The Right Dihedral shows a tectonic regime of strike-slip with extensional component (see De Vicente et al., 1992), with orthorhombic symmetry and S_{Hmax} oriented N10ºW, which is in agreement with the stress-tensor proposed by Herraiz et al. (2000) with $\sigma 2$ = 01°/355° and $\sigma 1$ vertical. However, strain analysis in this case shows a strike-slip extensional tectonic regime, instead of the extensional regime derived from the stress field. Despite this, both the Mohr-Coulomb analysis and the Paleostrain analysis (SM and RD), suggest N-S normal faulting, NNE-SSW to NE-SW and NNW-SSE to NW-SE strike-slips as the active fault network affecting the reservoir. De Vicente et al. (1992) pointed out that the SM analysis is more robust applied in fault-slip data classified previously by other techniques. Here, we have used the Mohr Coulomb failure criteria to separate active fault set under the same strain tensor, yielding robustness to the results from SM and RD analysis.

We propose as a complementary and future work, a combined analysis between the fault population analysis and the slip-tendency analysis (Morris et al. 1996), which could improve and discriminate those fault sets most likely to be reactivated under an active stress field. Although both analyses (Fault Population and slip-tendency) are based on the stress tensor and the orientation of fault traces, the slip-tendency also includes rock strength values obtained from the "in situ" tests.

5.2 Active faulting in the surrounding of HPP

Quaternary tectonic markers for the UFS are suggested by Tavani et al. (2011). According to the tectonic behavior of this fault as right-lateral strike-slip, and the fault segments proposed by Tavani et al. (2011), ranging between 12 and 14 km long, the question is whether this fault could trigger significant earthquakes and which could be the maximum associated magnitude. This is a relevant question given that the "natural seismicity" in the vicinity could affect the integrity of the caprock. Bearing in mind the expectable long-life for the reservoir, estimated in thousands of years, the potential natural earthquake that this master fault could trigger has to be estimated. In this sense, it is necessary to depict seismic scenarios related to large earthquake triggering; however, this type of analysis is beyond the focus of this work.

The income information that we have to manage in the area of influence (20 km) is: (a) the instrumental seismicity, (b) the geometry of the fault, (c) the total surface rupture, (d) the upper crust thickness and (e) the heat flow across the lithosphere. Starting for the heat flow value, the Hontomín wells show a value that lies between 62 and 78 mW/m^2 at a 1,500 m depth approximately (Fernández et al., 1998). Regarding the Moho depth in the area, these aforementioned authors obtained a value ranging between 36 and 40 km depth, while the lithosphere base ranges between 120 and 130 km depth (Torne et al., 2015). The relevance of this value is the study of the thermal weakness into the lithosphere that could nucleate earthquakes in intraplate areas (Holford et al., 2011). For these authors, the comparison between the crustal heat-flow in particular zones, in contrast with the background regional value, could explain large seismicity and high rates of small earthquakes occurrence, as the case of the New Madrid seismic zone (Landgraf et al., 2018). For example, in Australia heat-flow values as much as 90 mW/m^2 are related with earthquakes sized $M > 5$ (Holford et al., 2011).

Regarding the maximum expected earthquake into the zone, we have applied the empirical relationships obtained by Wells and Coppersmith (1994). We have used the equations for strike-slip earthquakes according to the strain field obtained in the area (pure shear), and the surface rupture segment for the Ubierna Fault System, assuming a surface rupture segments between 12 and 14 km (Tavani et al., 2011). The obtained results show that the maximum expected earthquake ranges between M 6.0 and M 6.1. Wells and Coppersmith (1994) indicate for these fault parameters a total area rupture ranging between 140 and 150 km^2. Surface fault traces rupture as lower as 7 km needs at least 20 km of depth in order to reach a value of the fault-area rupturing greater than 100 km^2, in line with a Moho between 36 and 40 in depth.

Regarding the instrumental earthquakes recorded into the area, the two largest earthquakes recorded correspond to magnitude M 3.4 and M 3.3, with a depth ranging between 8 and 11 km, respectively, and a felt macroseismic intensity of III (EMS98, www.ign.es, last access on May, 2019).Both earthquakes occurred between 50 and 60 km of distance from the Hontomín Pilot Plant. Only five earthquakes have been recorded within the 20-km radius area of influence and with small magnitudes ranging between M 1.5 and M 2.3. The interesting data is the depth of these earthquakes, ranging between 10 and 20 km, which suggest that the seismogenic crust could reach 20 km of depth.

5.3 Local tectonic field and induced seismicity

The fluid injection into a deep saline aquifer, which is used as GSC, generally increases the pore pressure. The increasing of the pore pressure migrates from the point of injection to the whole reservoir. Moreover, changes into the stress field for faults that are located below the reservoir, could also trigger induced earthquakes (Verdon et al., 2014). Nevertheless, to understand this possibility and the study the volumetric strain field spatial distribution is required (Lisle et al., 2009).

We have applied a physic model to estimate the total volume injected (room conditions) and in reservoir conditions. Then we have applied the McGarr's (2014) approximation of the maximum expected seismic moment for induced earthquakes. The injection of 10 k tons of CO_2 in Hontomín (Gastine et al., 2017), represents an approximated injected volume of CO_2 of 5.56 x10^6 m^3 (room conditions, pressure of 1 bar and temperature of 20 °C). The P/T conditions at the bottom of the wells have a maximum value close to 190 bar (Ortiz et al., 2015; Kovacs et al., 2015), although oscillating between 125 and 170 bar and with a maximum temperature close to 58 °C. Kovacs et al. (2015) pointed out a pressure gradient 0.023 MPa/m and a thermal vertical gradient of 0.033 °C/m, which would correspond to a pressure of 357 bar and a temperature of 51 °C at 1,550 m depth. P/T bottom values obtained from the observational wells (HA and HI) by Ortiz et al. (2015) and Kovacs et al. (2015), were 170 bar and 42 °C respectively.

We have used the general law for gases $P_1 * V_1/T_1 = P_2 * V_2/T_2$. Therefore, the total injected volume in reservoir conditions according to the parameters observed at the bottom of the wells are, P_1= 1.01 bar, T_1= 20 °C, V_1= 5.56 x 10^6 m^3, P_2= 170 bar and T_2= 42 °C. Hence, the total volume of injected CO_2 plus brine is 6.94 x 10^4 m^3.

McGarr (2014) empirically determined the maximum seismic moment related to a volume increasing by underground injection. The expression is Mo(max) (Nm) = G ·ΔV (McGarr 2014, eq. 13), where G is the modulus of rigidity and for the upper limit is 3 x 10^{10} Pa, and ΔV is the total injected volume (we have used the total injected volume in reservoir conditions). The result is Mo(max) equal to 2.1 x 10^{15} Nm, which corresponds to a maximum seismic moment magnitude Mw (max) = 4.2, by applying the equation Mw = (Log Mo(max) – 9.05)/1.5 from Hanks and Kanamori (1979); where Log is the logarithm to the base 10.

McGarr (2014) applied this approach for three cases: (1) wastewater injection, (2) hydraulic fracturing, and (3) geothermal injection. We propose to include this approach for fluid injection related to geological storage of CO_2. We assume that the pore pressure increases from CO_2 injection in a similar way that wastewater does (originally defined by Frohlich, 2012). According to McGarr (2014), the utility of the analysis we have performed is "to predict in advance of a planned injection whether there will be induced seismicity", and in the case of the HPP, to estimate of the "total injected volume" in a small-scale injection plant.

Therefore, the earthquake magnitude to this fluid-injected volume according to the McGarr (2014) and Verdon et al. (2014) could be M > 4 if there are faults with a minimum size of 4 km and oriented according to the present-day stress field (N-S extensional faults and NNE-SSW/NNW-SSE strike slip faults; **Fig. 10**). In the case of HPP, there are faults below the reservoir with this potential earthquake triggering (Alcalde et al., 2014). Also according to McGarr (2014), this value has not to be considered as an absolute physic limit but as a qualitative approximation. Alternatively, increasing by overpressure of the carbonate reservoir along with the pore pressure variations of about 0.5 MPa could trigger earthquakes, as well. Stress-drop related to fluid injections are also reported (Huang et al., 2016).

Le Gallo and de Dios (2018) described two main fault sets affecting the reservoir with N-S and E-W trend, respectively. According to the present-day stress tensor described by Herraiz et al. (2000) and Tavani et al. (2011), E-W fault-sets are accommodating horizontal shortening, which means that the permeability could be low. Besides, these faults are decoupled from the present-day stress tensor. However, N-S faults could act as normal faults and, hence, with higher permeability. In this sense, the study of focal mechanisms solutions could improve the safety management, even for microearthquakes of magnitude lesser than M 3.

Moreover, the CO_2 lateral diffusion and pressure variation change during the fluid injection phase, and then the system would relax before to be increased during the next injection phase. In this context, the intermittent and episodic injection of CO_2 could also trigger earthquakes by the stress-field and fluid pressure variations in short time periods.

6. CONCLUSIONS

The application of the analysis for brittle deformation determines the active tectonic strain field, applied in the ongoing seismic monitoring for Geological Carbon Storage (GSC). The possibility that pore pressure variations due to fluid injection could change the stress/strain conditions in the reservoir's caprock, makes the study of the present-day tectonic field as mandatory for the storage safety operations. In this sense, we have to bear in mind that this kind of subsurface storage is designed for long-life expectancy, about thousands of years, and therefore, relevant earthquakes could occur affecting the sealing and the seepage of CO_2, compromising the integrity of the reservoir. Hence, we can conclude from our analysis the following items:

(1) The study of the tectonic field allows classifying the geometry of the faults to prevent prone earthquake-related structures and design monitoring seismic network.

(2) The influence area around the facilities of the GSC for studying the active stress/strain field could reach 20 km from the facility, adding missing information from map scale and boreholes. This information could be used from the 3D local fracture pattern estimation to avoid the pore overpressure. Analysis of the stress-drop due to the fluid injection could be combined with this information to understand potential microseismicity associated with the injection operations.

(3) In the case of Hontomín Pilot-Plant, we have obtained two strain active tectonic fields featured as shear deformation. These fields are defined by (a) a local tectonic

strain field with e_y, S_{Hmax} striking N50ºE and (b) the regional one defined by e_y, S_{Hmax} with N150ºE trend. In this context, strike-slip faults with N-S, NNE-SSW and NNW-SSE trends, are accumulating present-day tectonic deformation. Analysis of Mohr-Coulomb failure criterion shows a potential reactivation of these fault sets.

(4) N-S faults are accumulating tectonic deformation and they could act as normal faults. This means that this fault set is the preferential direction for potential fluid leakage. In addition, intersection with NNE-SSW and NNW-SSE could arrange 3D networks for fluid mobilization and leakage.

(5) The Ubierna Fault System represents a tectonically active fault array that could trigger natural earthquakes as large as M 6 (±0.1), from the empirical relationship of the total rupture segment (ranging between 12 and 14 km, and the total fault-area rupture, oscillating between 100 and 150 km^2). Despite the lack of instrumental seismicity into the influence area, we cannot obviate the potential earthquake occurrence within intraplate areas due to the long- timescale expected-life of the GSC. The heat-flow values and thermal crust conditions could determine the presence of intraplate earthquakes with magnitude M > 5, for a long timescale (thousands of years), and the total injected fluid could trigger induced earthquakes greater than M 4.

The active strain field is now defined by an extensional tectonic defined by e_y with N-S trend, activating N-S normal faults and right-lateral faults with NNW- and NNE- trends.

Finally, we state that the determination of the active tectonic strain field, the application of the slip-tendency analysis, the recognition and study of active faults within the area of influence (20 km), the estimation of the maximum potential triggered natural earthquake, the modeling of the stress-change during the fluid injection and stress-drop, probably improve the operations for a secure storage. In a short future, earthquake scenarios will be the next step: modeling the Coulomb static stress-changes due to fluid injection and the modeling of intensity maps of horizontal seismic acceleration.

ACKNOWLEDGEMENTS

Thanks are given to Pr. Graham Yielding, Dr. Dave Haley, and an anonymous reviewer for their remarks during the open discussion. We wish to thank Pr. Allmendinger for the free use of the MohrPlotter 3.0 software, last access in March of 2020 at the web browser: http://www.geo.cornell.edu/geology/faculty/RWA/programs/mohrplotter.html This work has been partially supported by the European Project ENOS: ENabling Onshore CO_2 Storage in Europe, H2020 Project ID: 653718 and the Spanish project 3GEO, CGL2017-83931-C3-2-P, MICIU-FEDER. The authors would also thank the crew of CIUDEN at Hontomín facilities for their kind assistance during our fieldwork.

REFERENCES

Alcalde, J., Martí, D., Calahorrano, A., Marzan, I., Ayarza, P., Carbonell, R., Juhlin, C., and Pérez-Estaún, A.: Active seismic characterization experiments of the Hontomín research facility for geological storage of CO_2, Spain, Int. J. Greenh. Gas Con., 19, 785–795, http://dx.doi.org/10.1016/j.ijggc.2013.01.039, 2013.

Alcalde J., Marzán I., Saura E., Martí D., Ayarza P., Juhlin C., Pérez-Estaún, A., and Carbonell, R: 3D geological characterization of the Hontomín CO_2 storage site, Spain: Multidisciplinary approach from seismic, well-log and regional data, Tectonophysics, 627, 6–25, http://dx.doi.org/10.1016/j.tecto.2014.04.025, 2014.

Allmendinger, R. W., Cardozo, N. C., and Fisher, D.: Structural Geology Algorithms: Vectors & Tensors, Cambridge, England, Cambridge University Press, 289 pp, 2012.

Álvarez-Gómez, J. A.: FMC: a one-liner python program to manage, classify and plot focal mechanisms, EGU General Assembly, Vienna, Austria, 27 April-02 May, EGU2014-10887, 2014.

Anderson, E. M.: The Dynamics of Faulting and Dyke Formation with application to Britain, 2nd ed., Oliver and Boyd, Edinburgh, 206 pp., 1951.

Angelier, J.: Determination of the mean principal directions of stresses for a given fault population, Tectonophysics, 56, 17-26, https://doi.org/10.1016/0040-1951(79)90081-7, 1979.

Angelier, J.: Tectonic analysis of fault slip data sets, J. Geophys. Res., 89, 5835-5848, https://doi.org/10.1029/JB089iB07p05835, 1984.

Angelier, J.: Inversion of field data in fault tectonics to obtain the regional stress-III. A new rapid direct inversion method by analytical means, Geophys. J. Int., 103, 363-376, https://doi.org/10.1111/j.1365-246X.1990.tb01777.x, 1990.

Angelier, J. and Mechler, P.: Sur une méthode graphique de recherche des contraintes principales également utilisable en tectonique et en séismologie: la méthode des dièdres droits, B. Soc. Geol. Fr., 19, 1309-1318, http://dx.doi.org/10.2113/gssgfbull.S7-XIX.6.1309, 1977.

Aurell, M., Meléndez, G., Olóriz, F., Bádenas, B., Caracuel, J. E., García-Ramos, J. C., Goy, A., Linares, A., Quesada, S. and Robles, S.: Jurassic, in The geology of Spain, pp. 213–253, The Geological Society of London., 2002.

Bentham, M. and Kirby, G.: CO_2 Storage in Saline Aquifers. Oil Gas Sci. Technol., 60, 559-567, https://doi.org/10.2516/ogst:2005038, 2005.

Bott, M.H.P.: The mechanism of oblique-slip faulting, Geol. Mag., 96: 109-117. https://doi.org/10.1017/S0016756800059987, 1959.

Capote, R., De Vicente, G., and González Casado, J. M.: An application of the slip model of brittle deformation to focal mechanism analysis in three different plate tectonics situation. Tectonophysics, 191, 399-409, https://doi.org/10.1016/0040-1951(91)90070-9, 1991.

Calvet, F., Anglada, E. and Salvany, J. M.: El Triásico de los Pirineos, in Vera, J.A. (ed.) Geología de España, pp. 272–274, SGE–IGME, Madrid, 2004.

Carola, E.: The transition between thin-to-thick-skinned styles of deformation in the Western Pyrenean Belt. Ph. D. thesis, Universitat de Barcelona, 271 pp., 2004.

Christensen, N. P.: Report on the current state and need for further research on CO_2 capture and storage. CO2NET, European Carbon Dioxide Network, www.co2net.com, 2004.

Chu, S.: Carbon Capture and Sequestration, Science, 325, 1599, http://dx.doi.org/10.1126/science.1181637, 2009.

Dallmeyer, R. D. and Martínez-García, E., Eds.: Pre-Mesozoic Geology of Iberia, Springer-Verlag, Berlin Heidelberg, 1990.

De Vicente, G.: Análisis Poblacional de Fallas. El sector de enlace Sistema Central-Cordillera Ibérica. Ph. D. thesis, Universidad Complutense de Madrid, Spain, 317 pp., 1988.

De Vicente, G. Muñoz, A., Giner, J.L.: Use of the Right Dihedral Method: implications from the Slip Model of Fault Population Analysis, Rev. Soc. Geol. España, 5(3-4), 7-19. 1992.

De Vicente, G., Cloetingh, S., Muñoz-Martín, A., Olaiz, A., Stich, D., Vegas, R., Galindo-Zaldivar, J., and Fernández-Lozano, J.: Inversion of moment tensor focal mechanisms for active stresses around Microcontinent Iberia: Tectonic implications, Tectonics, 27: 1-22, http://dx.doi.org/10.1029/2006TC002093, 2008.

De Vicente, G., Cloetingh, S., Van Wees, J. D., and Cunha, P. P.: Tectonic classification of Cenozoic Iberian foreland basins, Tectonophysics, 502, 38–61, http://dx.doi.org/10.1016/j.tecto.2011.02.007, 2011.

Etchecopar, A., Vasseur, G., and Daignieres, M.: An inverse problem in microtectonics for the determination of stress tensor from fault striation analysis, J. Struct. Geol., 3, 51-65, http://dx.doi.org/10.1016/0191-8141(81)90056-0, 1981.

Fernández, M., Marzán, I., Correia, A., and Ramalho, E.: Heat flow, heat production, and lithospheric thermal regime in the Iberian Peninsula, Tectonophysics, 291, 29-53, http://dx.doi.org/10.1016/S0040-1951(98)00029-8, 1998.

Foulger, G. R., Wilson, M., Gluyas, J., Julian, B. R. and Davies, R.: Global review of human-induced earthquakes, Earth-Sci. Rev., 178, 438–514, http://dx.doi.org/10.1016/j.earscirev.2017.07.008, 2018.

Frohlich, C.: Two-year survey comparing earthquake activity and injection-well locations in the Barnett Shale, Texas. PNAS, vol. 109 (35), 13934 – 13938, https://doi.org/10.1073/pnas.1207728109, 2012.

García-Mondéjar, J., Pujalte, V. and Robles, S.: Características sedimentológicas, secuenciales y tectoestratigráficas del Triásico de Cantabria y norte de Palencia, Cuad. Geol. Ibérica, (10), 151–172, 1986.

García-Mondéjar, J., Agirrezabala, L. M., Aranburu, A., Fernández-Mendiola, P. A., Gómez-Pérez, I., López-Horgue, M. and Rosales, I.: Aptian-Albian tectonic pattern of the Basque-Cantabrian Basin (Northern Spain), Geological Journal, 31(1), 13–45, http://dx.doi.org/10.1002/(SICI)1099-1034(199603)31:1<13::AID-GJ689>3.0.CO;2-Y, 1996.

Gastine, M., Berenblyum, R., Czernichowski-lauriol, I., de Dios, J. C., Audigane, P., Hladik, V., Poulsen, N., Vercelli, S., Vincent, C., and Wildenborg, T.: Enabling onshore CO_2 storage in Europe: fostering international cooperation around pilot and test sites, Energy Proced., 114, 5905–5915, http://dx.doi.org/10.1016/j.egypro.2017.03.1728, 2017.

Giner-Robles, J.L., Pérez-López, R., Elez, J., Silva, P.G., Rodríguez Escudero, E., Canora, C., Rodríguez-Pascua, M.A., Bardají, T., Roquero, E., Huerta, P., Perucha, M.A.: Strain analysis in the Iberian Peninsula from focal mechanism solutions, seismic hazard impacts, In: C. Canora, F. Martín, E. Masana, R. Pérez y M. Ortuño, Eds., pp. 249-252. Tercera reunión ibérica sobre fallas activas y paleosismología, Alicante (España), 2018.

Goldberg, D. S., Kent, D. V., and Olsen, P. E.: Potential on-shore and off-shore reservoirs for CO_2 sequestration in Central Atlantic magmatic province basalts, P. Natl. Acad. Sci. USA, 107, 1327–1332, http://dx.doi.org/10.1073/pnas.0913721107, 2010.

Gómez, M., Vergés, J. and Riaza, C.: Inversion tectonics of the northern margin of the Basque Cantabrian Basin, Bulletin de la Société Géologique de France, 173(5), 449–459, http://dx.doi.org/10.2113/173.5.449, 2002.

Goodman, R. E.: Introduction to Rock Mechanics, 2nd Edition, John Wiley & Sons, Inc., New York. 576 pp., 1989.

Hanks, T.C., Kanamori, H.: A Moment Magnitude Scale, J. Geophys. Res., 84 (B5), 2348–2350, https://doi.org/10.1029/JB084iB05p02348, 1979.

Herraiz, M., De Vicente, G., Lindo-Naupari, R., Giner, J., Simón, J.L., González-Casado, J.M., Vadillo, O., Rodríguez-Pascua, M.A., Cicuéndez, J.I., Casas, A., Cabañas, L., Rincón, P., Cortés, A.L., Ramírez, M., and Lucini, M.: The recent (upper Miocene to Quaternary) and present tectonic stress distributions in the Iberian Peninsula, Tectonics, 19, 762–786, https://doi.org/10.1029/2000TC900006, 2000.

Holford, S. M., Hillis, R. R., Hand, M., and Sandiford, M.: Thermal weakening localizes intraplate deformation along the southern Australian continental margin, Earth Planet. Sc. Lett., 305, 207–214, http://dx.doi.org/10.1016/j.epsl.2011.02.056, 2011.

Huang, Y., Beroza, G. C., and Ellsworth, W. L.: Stress drop estimates of potentially induced earthquakes in the Guy-Greenbrier sequence, J. Geophys. Res.-Sol. Ea., 121, 6597–6607, http://dx.doi.org/10.1002/2016JB013067, 2016.

Kaverina, A. N., Lander, A. V., and Prozorov, A. G.: Global creepex distribution and its relation to earthquake-source geometry and tectonic origin, Geophys. J. Int., 125, 249-265, https://doi.org/10.1111/j.1365-246X.1996.tb06549.x, 1996.

Kovacs, T., Poulussen, D.F. and de Dios, C.: Strategies for injection of CO_2 into carbonate rocks at Hontomin. Final Technical Report, Global Carbon Capture and Storage Institute Ltd. 2015. 66p. https://www.globalccsinstitute.com/archive/hub/publications/193428/strategies-injection-co2-carbonate-rocks-hontomin-final-technical-report.pdf, 2015.

Labuz, J. F., Zang, A.: Mohr–Coulomb Failure Criterion. Rock Mech. Rock Eng., 45, 975–979, https://doi.org/10.1007/s00603-012-0281-7, 2012.

Landgraf, A., Kuebler, S., Hintersberger, E., Stein, S.: Active tectonics, earthquakes and palaeoseismicity in slowly deforming continents, Landgraf, A., Kuebler, S., Hintersberger, E. & Stein, S. (eds) Seismicity, Fault Rupture and Earthquake Hazards in Slowly Deforming Regions. Geological Society, London, Special Publications, 432, http://doi.org/10.1144/SP432.13, 2018.

Le Gallo, Y. and de Dios, J. C.: Geological Model of a Storage Complex for a CO_2 Storage Operation in a Naturally-Fractured Carbonate Formation, Geosciences, 2018, 8, 354, http://dx.doi.org/10.3390/geosciences8090354, 2018.

Le Pichon, X. and Sibuet, J.-C.: Western extension of boundary between European and Iberian plates during the Pyrenean orogeny, Earth and Planetary Science Letters, 12(1), 83–88, http://dx.doi.org/10.1016/0012-821X(71)90058-6, 1971.

Lepvrier, C. and Martínez-García, E.: Fault development and stress evolution of the post-Hercynian Asturian Basin (Asturias and Cantabria, northwestern Spain), Tectonophysics, 184, 345, http://dx.doi.org/10.1016/0040-1951(90)90447-G, 1990.

Lisle, R. J., Aller, J., Bastida, F., Bobillo-Ares, N. C., and Toimil, N. C.: Volumetric strains in neutral surface folding, Terra Nova, 21, 14–20, http://dx.doi.org/10.1111/j.1365-3121.2008.00846.x, 2009.

McGarr, A.: Maximum magnitude earthquakes induced by fluid injection, J. Geophys. Res., 119, 1008–1019, https://doi.org/10.1002/2013JB010597, 2014.

McNamara, D.D. Methods and techniques employed to monitor induced seismicity from carbon capture and storage, GNS Science Report 2015/18, 23 pp., http://dx.doi.org/10.13140/RG.2.2.13830.98888, 2016.

Morris, A., Ferrill, D. A. and Henderson, D. B.: Slip-tendency analysis and fault reactivation, Geology, 24, 275-278, http://doi.org/10.1130/0091-7613(1996)024<0275:STAAFR>2.3.CO;2, 1996.

Muñoz, J. A.: Evolution of a continental collision belt: ECORS-Pyrenees crustal balanced cross-section, in Thrust Tectonics, edited by K. R. McClay, pp. 235–246, Springer Netherlands, Dordrecht., 1992.

Ogaya, X., Ledo J., Queralt P., Marcuello, A., and Quintà, A.: First geoelectrical image of the subsurface of the Hontomín site (Spain) for CO_2 geological storage: A magnetotelluric 2D characterization, Int. J. Greenh. Gas Con., 13, 168–179, https://dx.doi.org/10.1016/j.ijggc.2012.12.023, 2013.

Orr, F.M.: Onshore Geologic Storage of CO_2, Science, 325, 1656-1658, http://dx.doi.org/10.1126/science.1175677, 2009.

Ortiz, G., Kovacs, T., Poulussen, D.F. and de Dios, C.: Hontomin reservoir characterisation test, Final Technical Report. Global Carbon Capture and Storage Institute Ltd. 2015. 48p. https://www.globalccsinstitute.com/resources/publications-reports-research/?filter=2015-05-01,2015-07-25&type=date, 2015.

Pan, P., Wu, Z., Feng, X., Yan, F.: Geomechanical modeling of CO_2 geological storage: A review, J. Rock Mech. and Geotech. Eng., 8, 936-947, http://dx.doi.org/10.1016/j.jrmge.2016.10.002, 2016.

Pérez-López, R., Mediato, J.F., Rodríguez-Pascua, M.A., Giner-Robles, J.L., Martínez-Orío, R., Arenillas-González, A., Fernández-Canteli, P., de Dios, J.C., Loubeau, L.: Aplicación del análisis estructural y campos de deformación para el estudio de sismicidad inducida en almacenamiento profundo: Hontomín, In: C. Canora, F. Martín, E. Masana, R. Pérez y M. Ortuño, Eds., pp. 279-282. Tercera reunión ibérica sobre fallas activas y paleosismología, Alicante (España), 2018.

Pearce, J. M.: What can we learn from Natural Analogues? An overview of how analogues can benefit the geological storage of CO_2, in: Advances in the Geological Storage of Carbon Dioxide, edited by: Lombardi, S., Altunina, L. K., and Beaubien, S. E., Springer, Dordrecht, The Netherlands, 129–139, 2005.

Pegoraro, O.: Application de la microtectonique à un étude de neotectonique. Le golfe Maliaque (Grèce centrale). Ph.D. thesis, U.S.T.L. Montpellier, France, 41 pp., 1972.

Permentier, K., Vercammen, S., Soetaert, S., and Schellemans, Ch.: Carbon dioxide poisoning: a literature review of an often forgotten cause of intoxication in the emergency department, International Journal of Emergency Medicine, 10, 14, http://dx.doi.org/10.1186/s12245-017-0142-y, 2017.

Quintà, A. and Tavani S., The foreland deformation in the south-western Basque–Cantabrian Belt (Spain), *Tectonophysics*, 576–577, 4–19, http://dx.doi.org/10.1016/j.tecto.2012.02.015, 2012.

Reches, Z.: Faulting of rocks in three-dimensional strain fields, II. Theoretical analysis, Tectonophysics, 95, 133-156, https://doi.org/10.1016/0040-1951(83)90264-0, 1983.

Reches, Z.: Determination of the tectonic stress tensor from slip along faults that obey the Coulomb yield condition, Tectonics, 7, 849-861, https://doi.org/10.1029/TC006i006p00849, 1987.

Rice, S. A.: Health effects of acute and prolonged CO_2 exposure in normal and sensitive populations, Second Annual Conference on Carbon Sequestration, Alexandria, Virginia, USA, 5-6 May, 2003.

Roca, E., Muñoz, J. A., Ferrer, O. and Ellouz, N.: The role of the Bay of Biscay Mesozoic extensional structure in the configuration of the Pyrenean orogen: Constraints from the MARCONI deep seismic reflection survey, Tectonics, 30(2), https://10.1029/2010TC002735, 2011.

Röhmann, L., Tillner, E., Magri, F., Kühn, M., and Kempka, T.: Fault reactivation and ground surface uplift assessment at a prospective German CO_2 storage site, Energy Proced., 40, 437–446. http://dx.doi.org/10.1016/j.egypro.2013.08.050, 2013.

Scholz, C.: The seismic cycle. In The Mechanics of Earthquakes and Faulting 3rd edition, Cambridge, Cambridge University Press, pp. 228-277, 2018.

Serrano, A. and Martínez del Olmo, W.: Tectónica salina en el Dominio Cantabro–Navarro: evolución, edad y origen de las estructuras salinas, in: Formaciones evaporíticas de la Cuenca del Ebro y cadenas perifericas, y de la zona de Levante, edited by: Orti, F. and Salvany, J.M., Empresa Nacional De Residuos Radiactivos S.A, ENRESA-GPPG, Barcelona, Spain, 39–53, 1990.

Simpson, R. S.: Quantifying Anderson's fault types, J. Geophys. Res., 102, 17,909-17,919, https://doi.org/10.1029/97JB01274, 1997.

Stich, D., Serpelloni, E., Mancilla, F. L., and Morales, J.: Kinematics of the Iberia-Maghreb plate contact from seismic moment tensors and GPS observations, Tectonophysics, 426, 295-317. https://doi.org/10.1016/j.tecto.2006.08.004, 2006.

Soto R., Casa-Sainz A. M., and Villalaín, J. J.: Widespread Cretaceous inversion event in northern Spain: evidence form subsurface and palaeomagnetic data, Journal of the Geological Society London, 168, 899-912, http://dx.doi.org/10.1144/0016-76492010-072, 2011.

Tavani, S., Quintá, A., and Granado, P.: Cenozoic right-lateral wrench tectonics in the Western Pyrenees (Spain): The Ubierna Fault System, Tectonophysics, 509, 238-253, http://dx.doi.org/10.1016/j.tecto.2011.06.013, 2011.

Tavani, S.: Plate kinematics in the Cantabrian domain of the Pyrenean orogeny, Solid Earth, 3, 265–292, http://dx.doi.org/10.5194/se-3-265-2012, 2012.

Tavani, S., Carola, C., Granado, P., Quintà, A., and Muñoz, J. A.: Transpressive inversion of a Mesozoic extensional forced fold system with an intermediate décollement level in the Basque - Cantabrian Basin (Spain), Tectonics, 32, http://dx.doi.org/10.1002/tect.20019, 2013.

Torne, M., Fernàndez, M., Vergés, J., Ayala, C., Salas, M. C., Jimenez-Munt, I., Buffett, G. G., and Díaz, J.: Crust and mantle lithospheric structure of the Iberian Peninsula deduced from potential field modeling and thermal analysis, Tectonophysics, 663, 419–433, http://dx.doi.org/10.1016/j.tecto.2015.06.003, 2015.

Tugend, J., Manatschal, G., Kusznir, N. J., Masini, E., Mohn, G. and Thinon, I.: Formation and deformation of hyperextended rift systems: Insights from rift domain mapping in the Bay of Biscay-Pyrenees, Tectonics, 33(7), 1239–1276, http://dx.doi.org/10.1002/2014TC003529, 2014.

Vegas, R., Vázquez, J. T., Olaiz, A. J., and Medialdea, T.: Tectonic model for the latest Triassic - Early Jurassic extensional event in and around the Iberian Peninsula, Geogaceta, 60, 23-26, 2016.

Verdon, J. P.: Significance for secure CO_2 storage of earthquakes induced by fluid injection, Environ. Res. Lett., 9, 064022 (10pp), http://dx.doi.org/10.1088/1748-9326/9/6/064022, 2014.

Verdon, J. P., Stork, A. L., Bissell, R. C., Bond, C. E., and Werner, M. J.: Simulation of seismic events induced by CO_2 injection at In Salah, Algeria, Earth Planet. Sci. Lett., 426, 118–129, http://dx.doi.org/10.1016/j.epsl.2015.06.029, 2015.

Vergés, J., Fernández, M. and Martínez, A.: The Pyrenean orogen: pre-, syn-, and post-collisional evolution, J. Virt. Ex, 08, http://dx.doi.org/10.3809/jvirtex.2002.00058,2002.

Wells, D. L. and Coppersmith, K. J.: New empirical relationships among magnitude, rupture length, rupture width, rupture area, and surface displacement, B. Seismol. Soc. Am., 84, 974–1002, 1994.

Wilson, M. P., Foulger, G. R., Gluyas, J. G., Davies, R. J., and Julian, B. R.: HiQuake the human-induced earthquake database, Seismol. Res. Lett., 88, 1560-1565, http://dx.doi.org/10.1785/0220170112, 2017.

Winthaegen, P., Arts, R., and Schroot, B.: Monitoring Subsurface CO_2 Storage. Oil Gas Sci. Technol., 60, 573-582, 2005.

Xu, S.-S., A.F. Nieto-Samaniego, S.A. Alaniz-Álvarez: 3D Mohr diagram to explain reactivation of pre-existing planes due to changes in applied stresses, Rock Stress and Earthquakes – Xie (ed.), 739-745 p, 2010.

Žalohar, J. and Vrabec, M.: Combined kinematic and paleostress analysis of fault-slip data: The Multiple-slip method, J. Struct. Geol., 30, 1603–1613, http://dx.doi.org/10.1016/j.jsg.2008.09.004, 2008.

FIGURE CAPTIONS

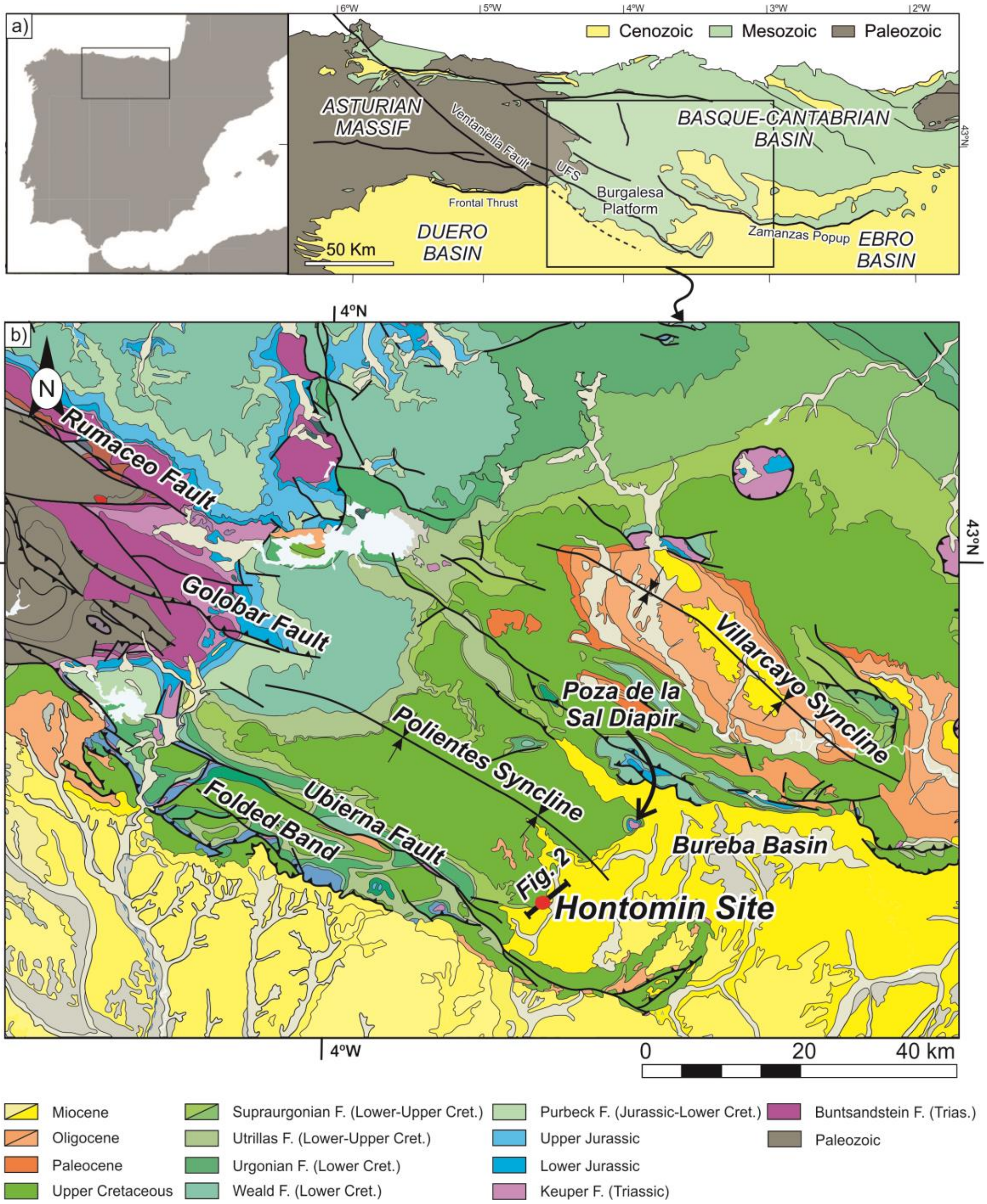

Figure 1. a) Location map of the study area in the Iberian Peninsula, along with the geological map of the Asturian and Basque-Cantabrian areas, labelling major units and faults (modified after Quintà and Tavani 2012); b) Geographical location of Hontomín pilot-plant (red dot) within the Basque-Cantabrian Basin. This basin is tectonically controlled by the Ubierna Fault System (UFS; NW-SE oriented) and the parallel Polientes syncline, the Duero and Ebro Tertiary basins and Poza de la Sal evaporitic diapir. Cret: Cretaceous; F: Facies.

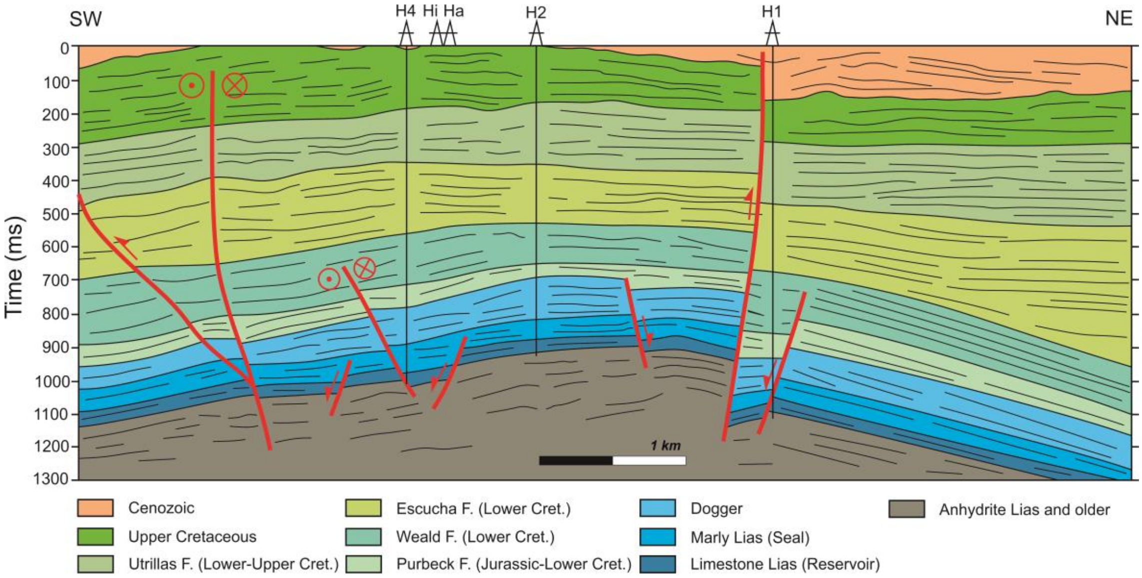

Figure 2. Interpretation of a 2D seismic reflection profile crossing the oil exploration wells (H1, H2 and H4), along with the monitoring well (Ha) and injection well (Hi) through Hontomin Pilot Plant (HPP). Modified from Alcalde et al. (2014). See Figure 1 for location, black line at the red circle.

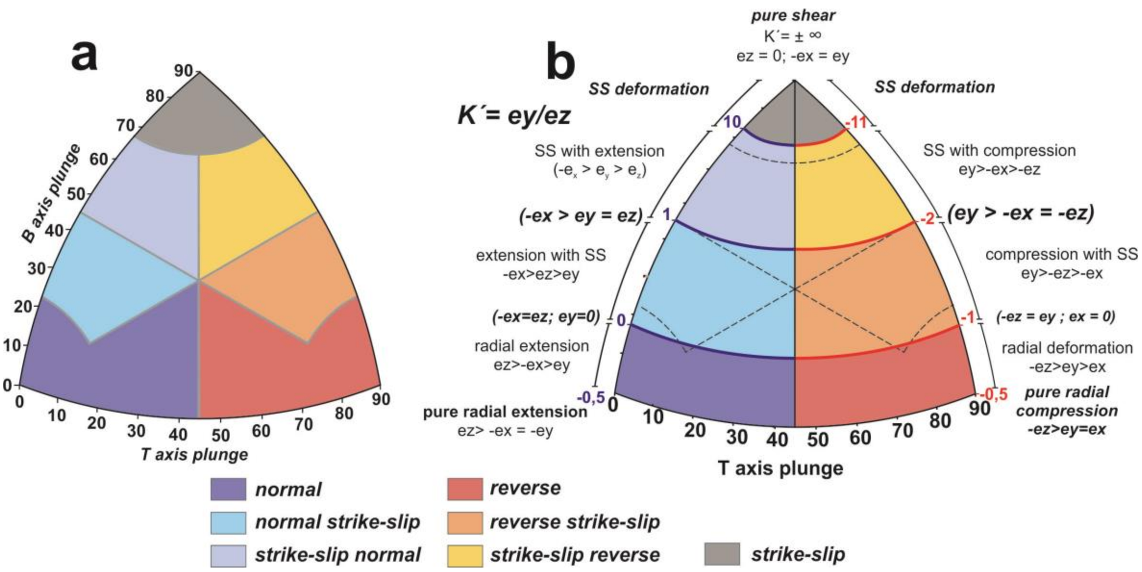

Figure 3. a) Kaverina original diagram to represent the tectonic regime from an earthquake focal mechanism population (see Kaverina et al., 1996 and Álvarez-Gómez, 2014). b) K'-strain diagram used in this work. Dotted lines represent the original Kaverina limits. Colored zones represent the type of fault. The tectonic regime is also indicated by the relationship between the strain axes and the colored legend. SS Strike slip. The B axis is the orthogonal to the P and T axes.

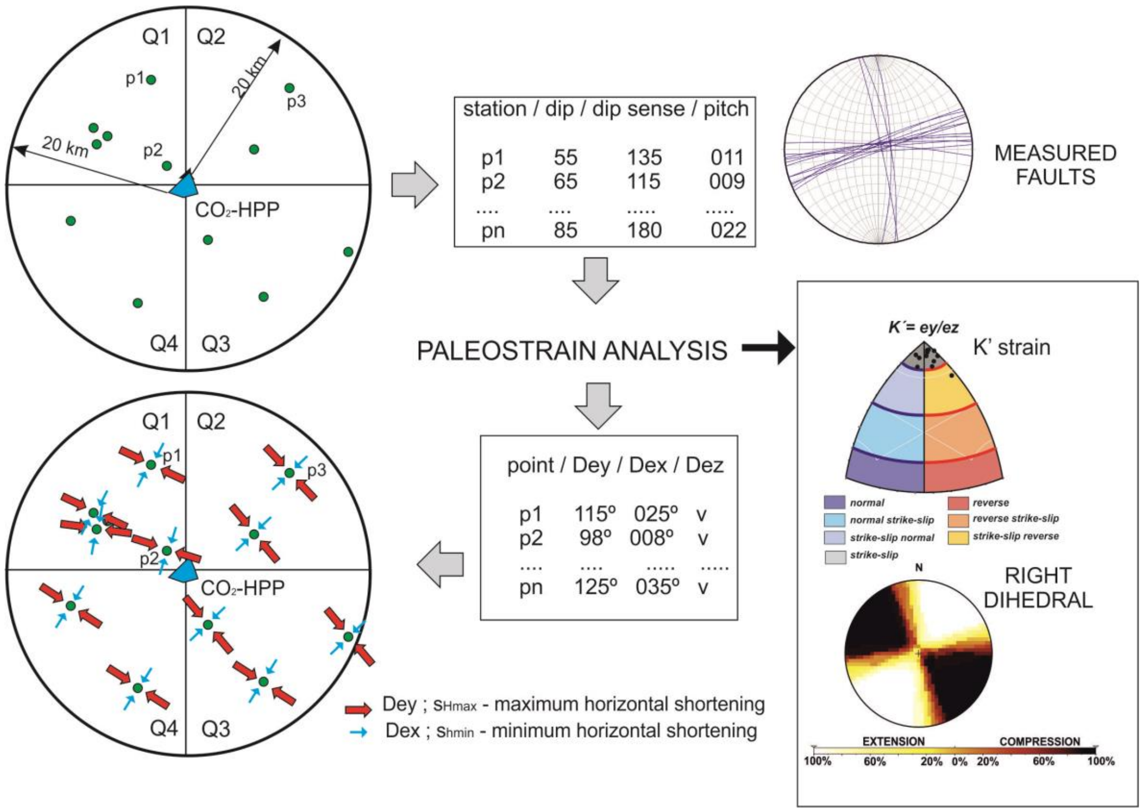

Figure 4. Methodology proposed to obtain the strain field affecting the GSC reservoir. The distances for outcrops and quadrants proposed is 20 km. The technique of Right Dihedral and the K' strain diagram is described in the main text. The ey and ex represented are a model for explaining the methodology. Dey and Dex are the direction of the maximum and minimum strain, respectively. Blue box at the center is the CO_2 storage geological underground formation.

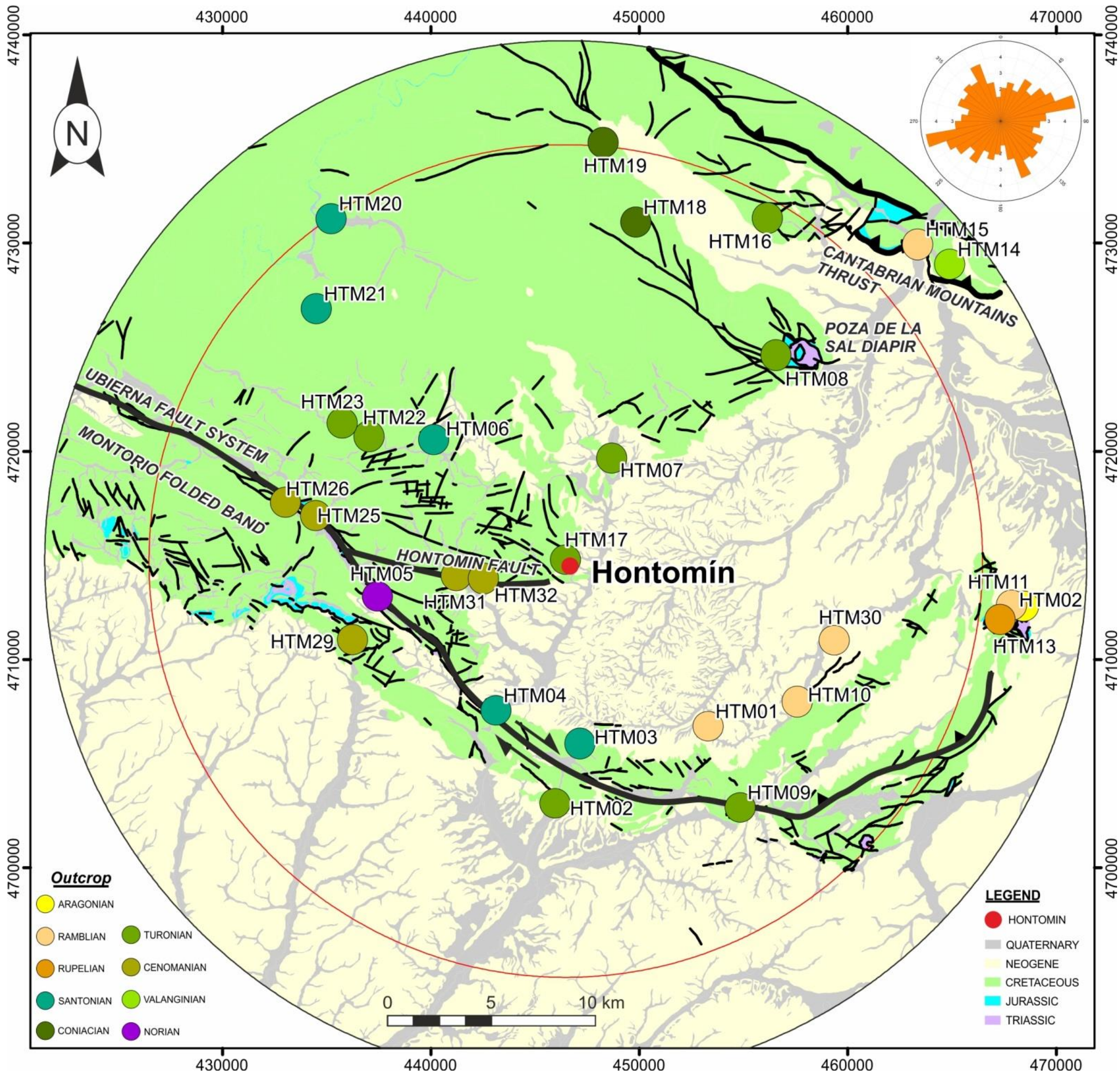

Figure 5. Geographical location of field outcrops in the eastern part of the Burgalesa Platform domain. Black lines: observed faults; red circle: 20km radius study zone. Rosd diagram are the fault orientations from the map. A total of 447 fault data were collected in 32 outcrops. Data were measured by a tectonic compass on fault planes at outcrops. The spatial distribution of the field stations is constrained by the lithology. Coordinates are in meters, UTM H30.

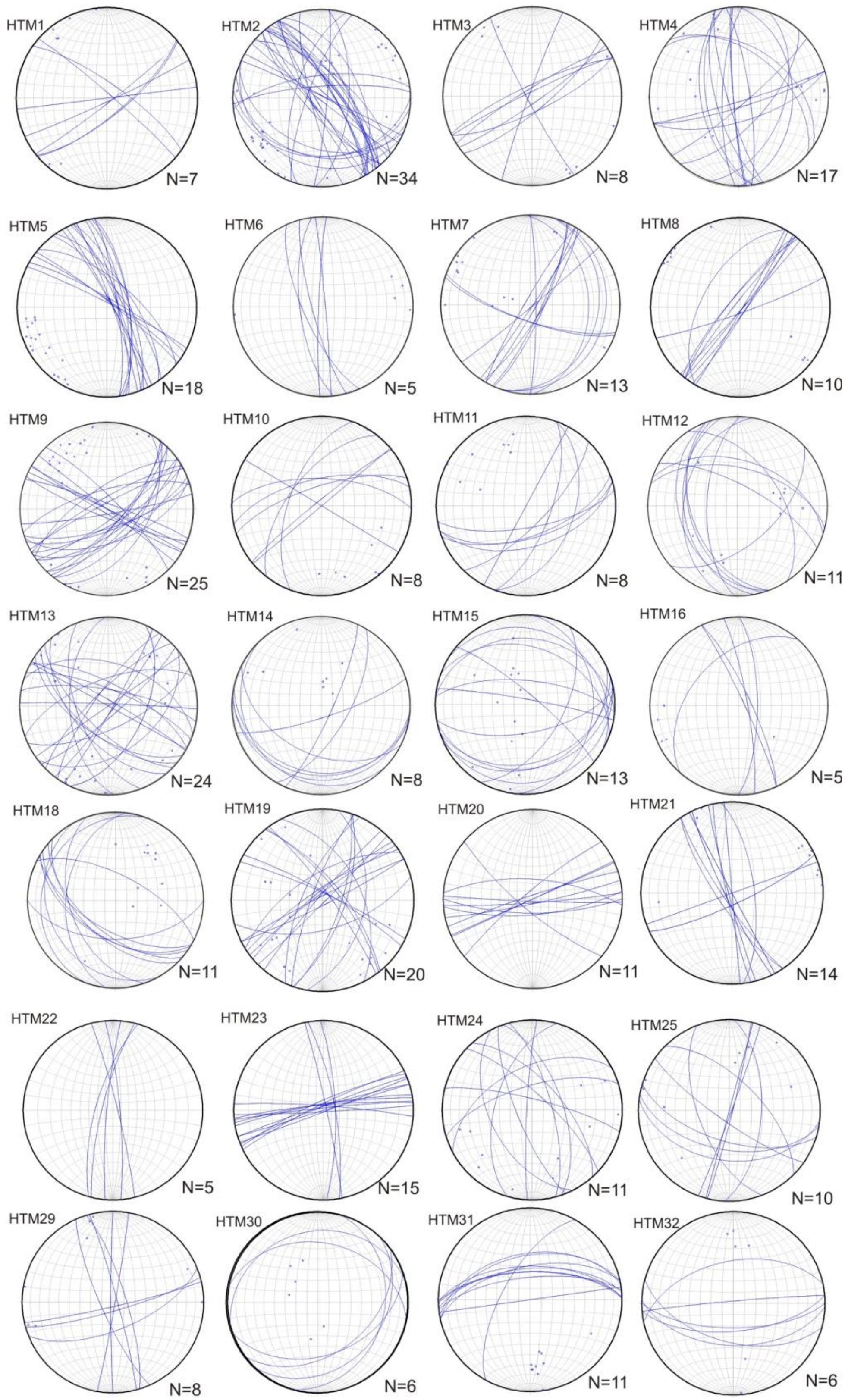

Figure 6. Stereographic representation (cyclographic plot in Schmidt net, lower hemisphere) of the fault planes measured in the field stations. “n” is the number of available data for each geoestructural station. HTM24, 27, 28 are not included due to lack of data, and HTM17 due to the high number of faults.

1055

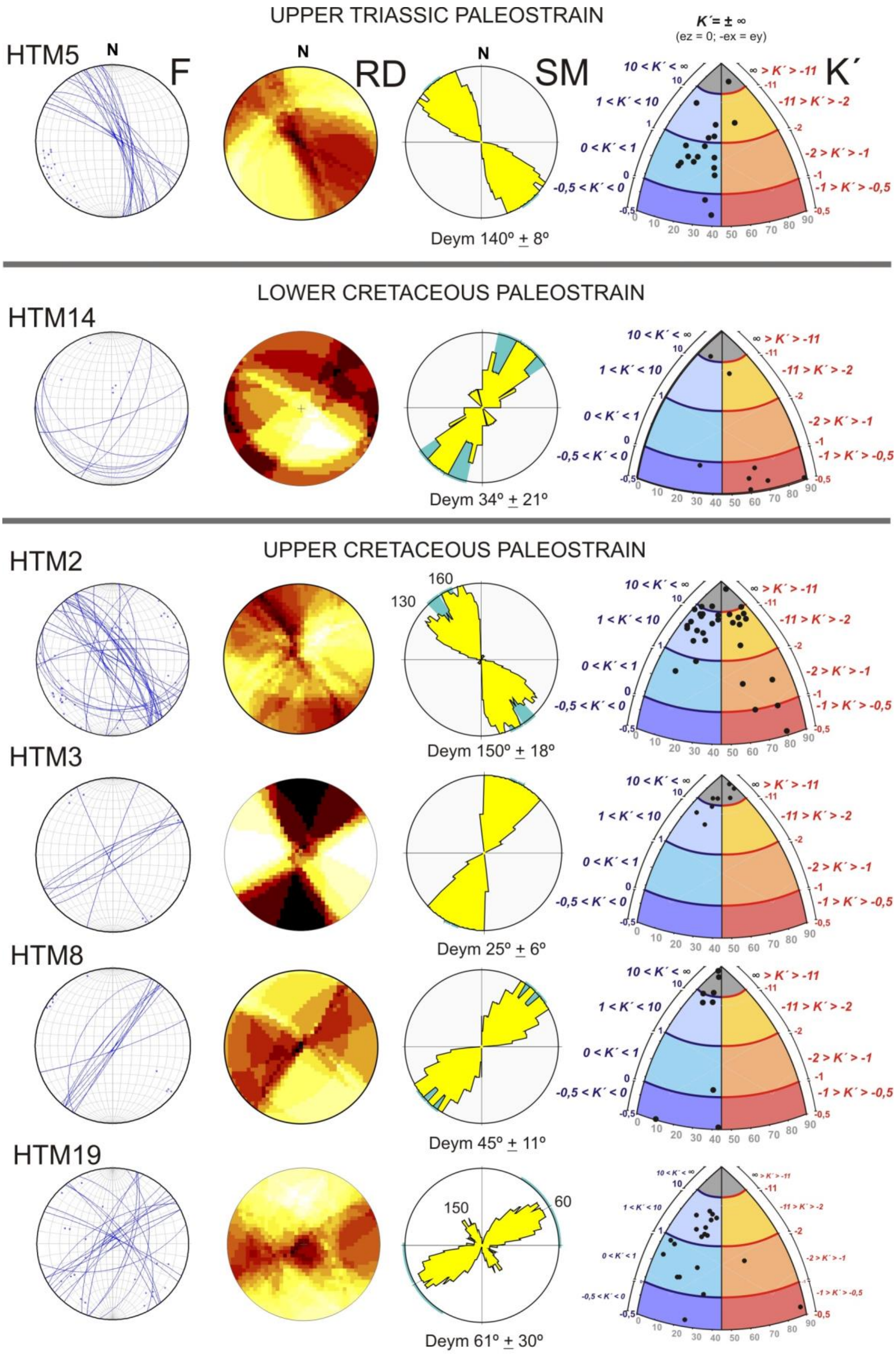

1056

FIGURE 7a

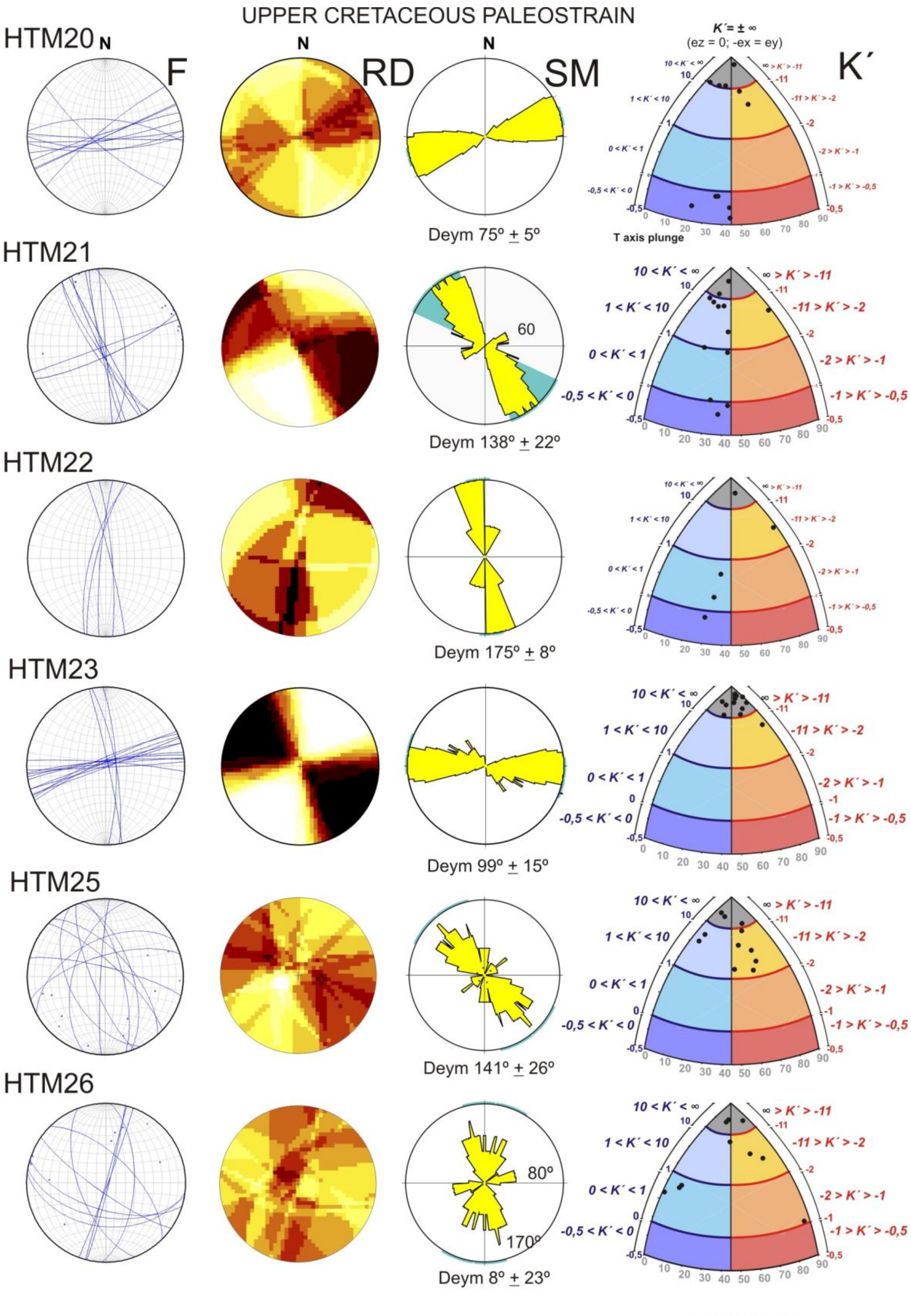
UPPER CRETACEOUS PALEOSTRAIN
HTM20
N
F
RD
SM
K´
K´= ± ∞
(ez = 0; -ex = ey)
Deym 75º ± 5º
T axis plunge
HTM21
60
Deym 138º ± 22º
HTM22
Deym 175º ± 8º
HTM23
Deym 99º ± 15º
HTM25
Deym 141º ± 26º
HTM26
80º
170º
Deym 8º ± 23º
10 < K´ < ∞
1 < K´ < 10
0 < K´ < 1
-0,5 < K´ < 0
∞ > K´ > -11
-11 > K´ > -2
-2 > K´ > -1
-1 > K´ > -0,5

FIGURE 7b

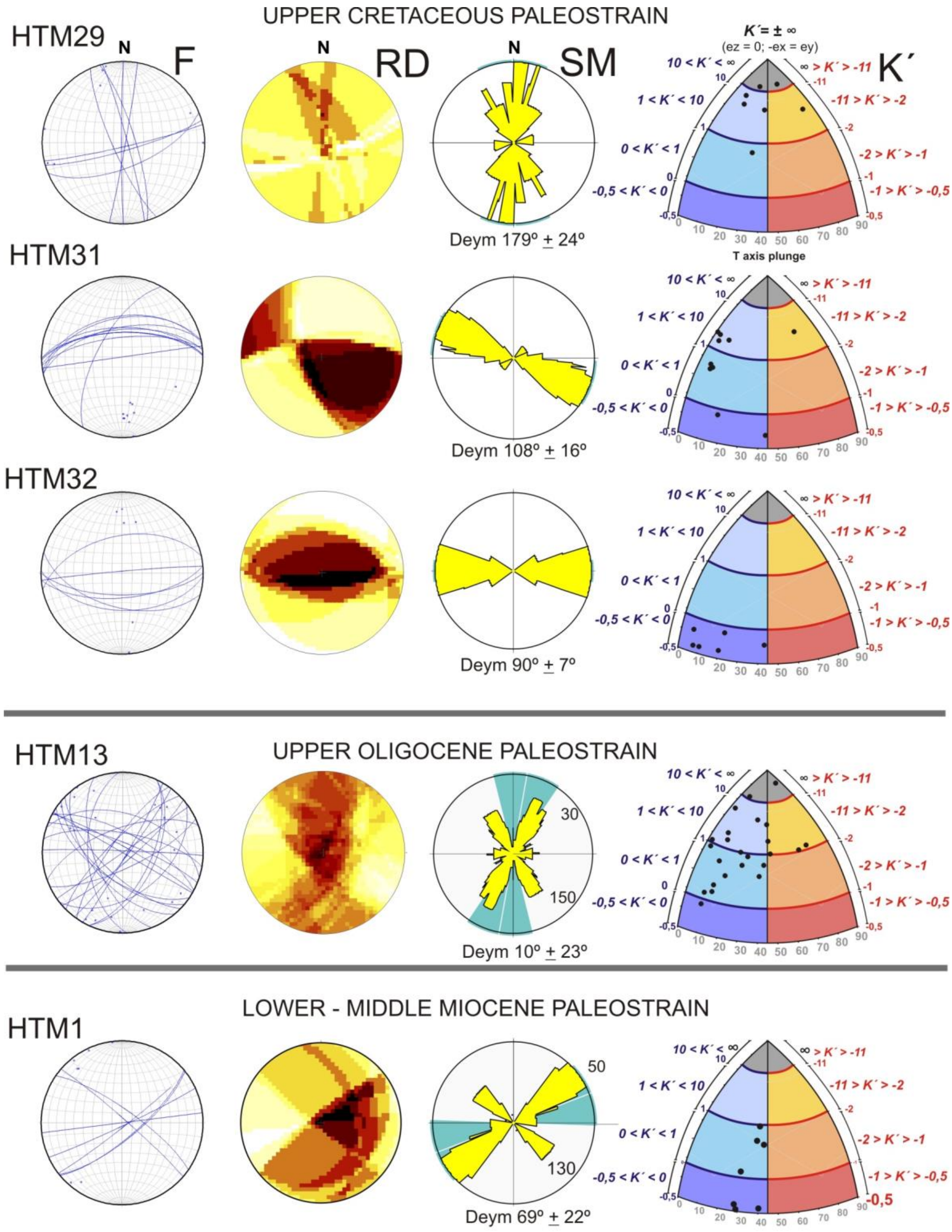

1061 **FIGURE 7c**

1062

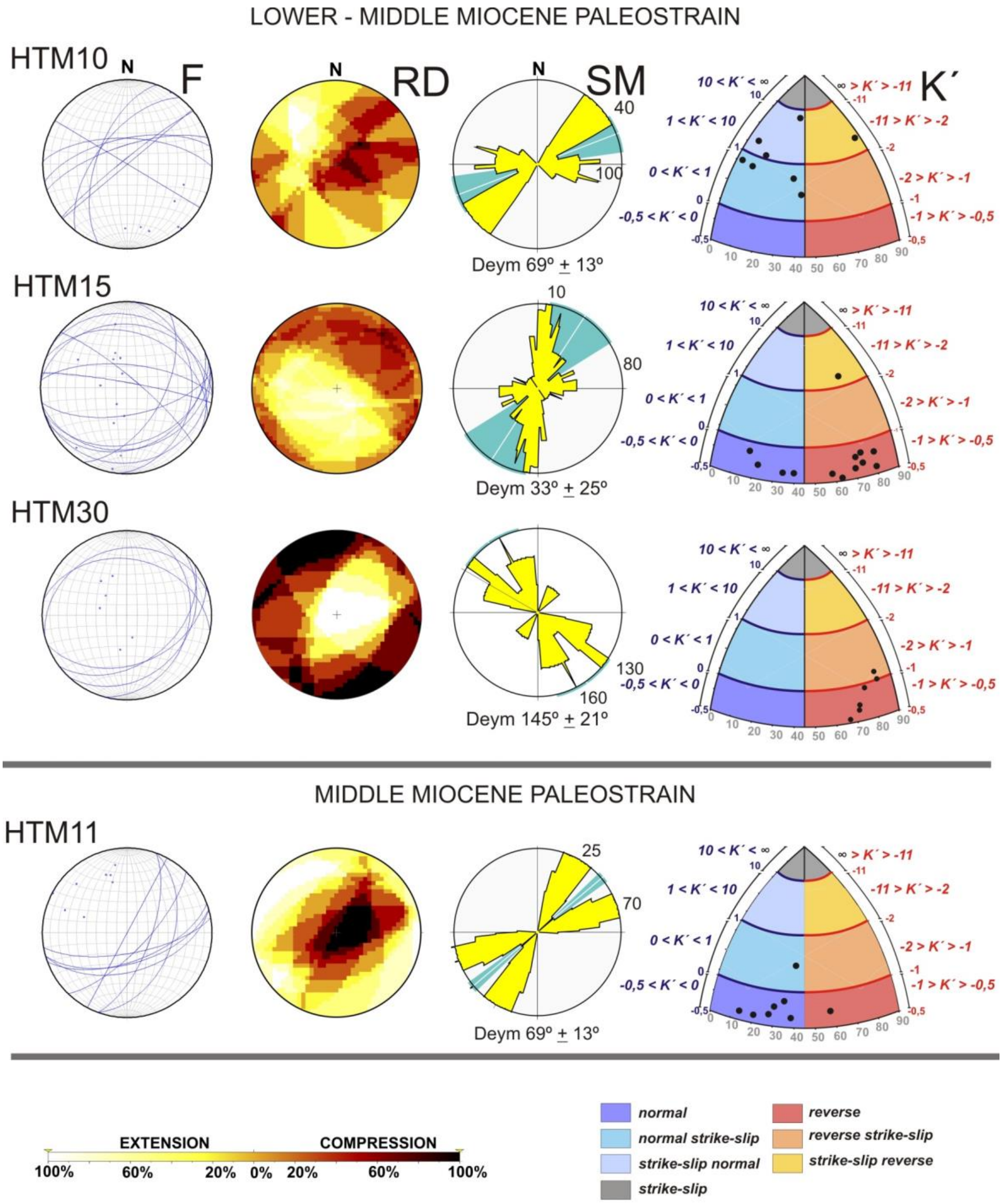

FIGURE 7d

Figure 7. Results of the paleostrain analysis obtained and classified by age. Deym: striking of the averaged of the Dey value; F: fault stereographic representation; K': diagram with dots for each fault slip solution; RD: Right Dihedral method; SM: Slip Method, K'. See Methods for further explanation.

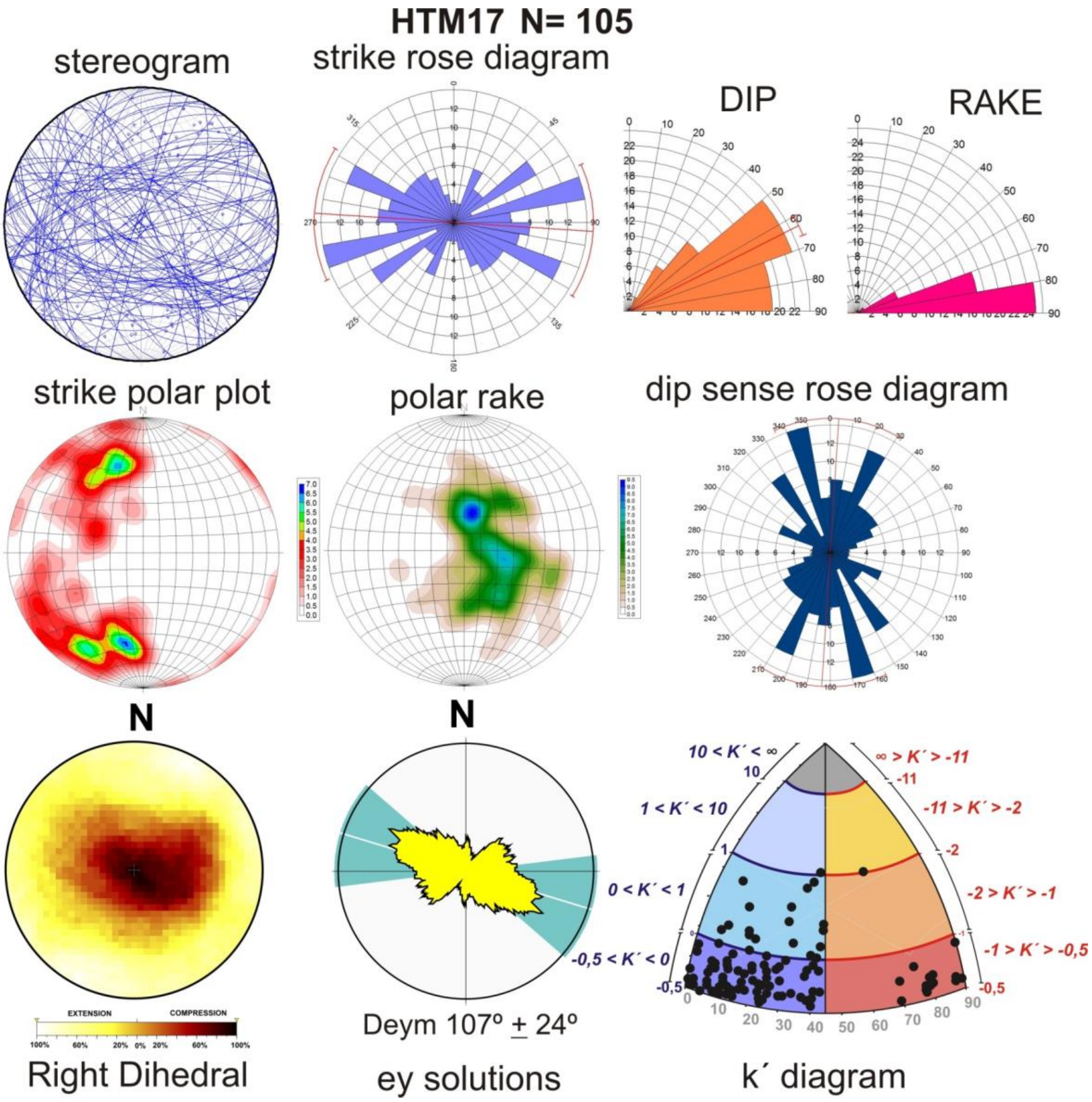

Figure 8. Fault data from the outcrop HTM17 located on top of the HPP. See figure 5 for the geographical location. Stereogram plot is lower hemisphere and Schmidt net.

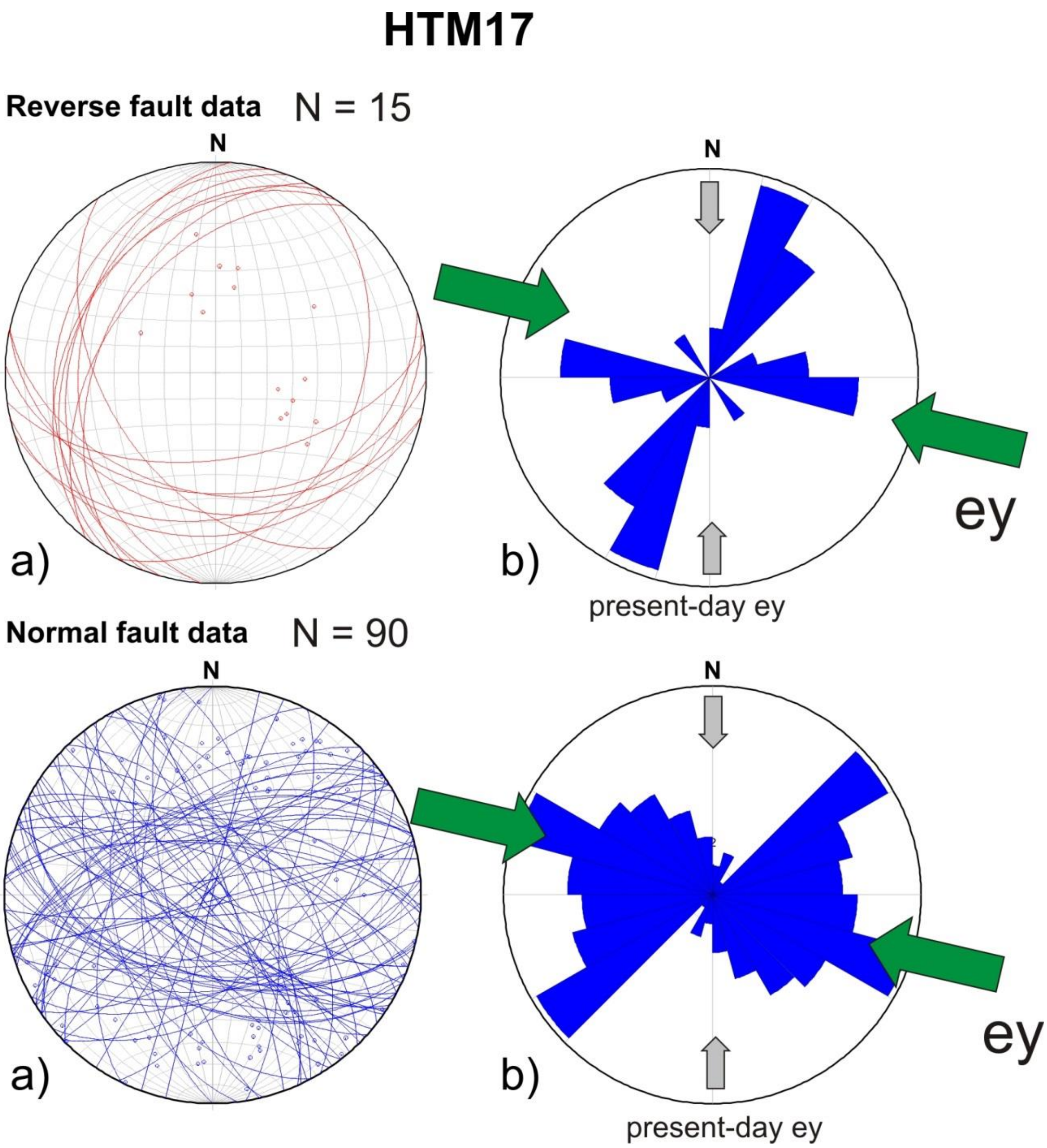

Figure 9. Normal and reverse faults stereograms (lower hemisphere and Schmidt net), and rose diagrams measured in HTM17. Green arrows indicate the orientation of the local paleostrain field. Grey arrows indicate the orientation of the present-day regional stress field (Herraiz et al., 2000).

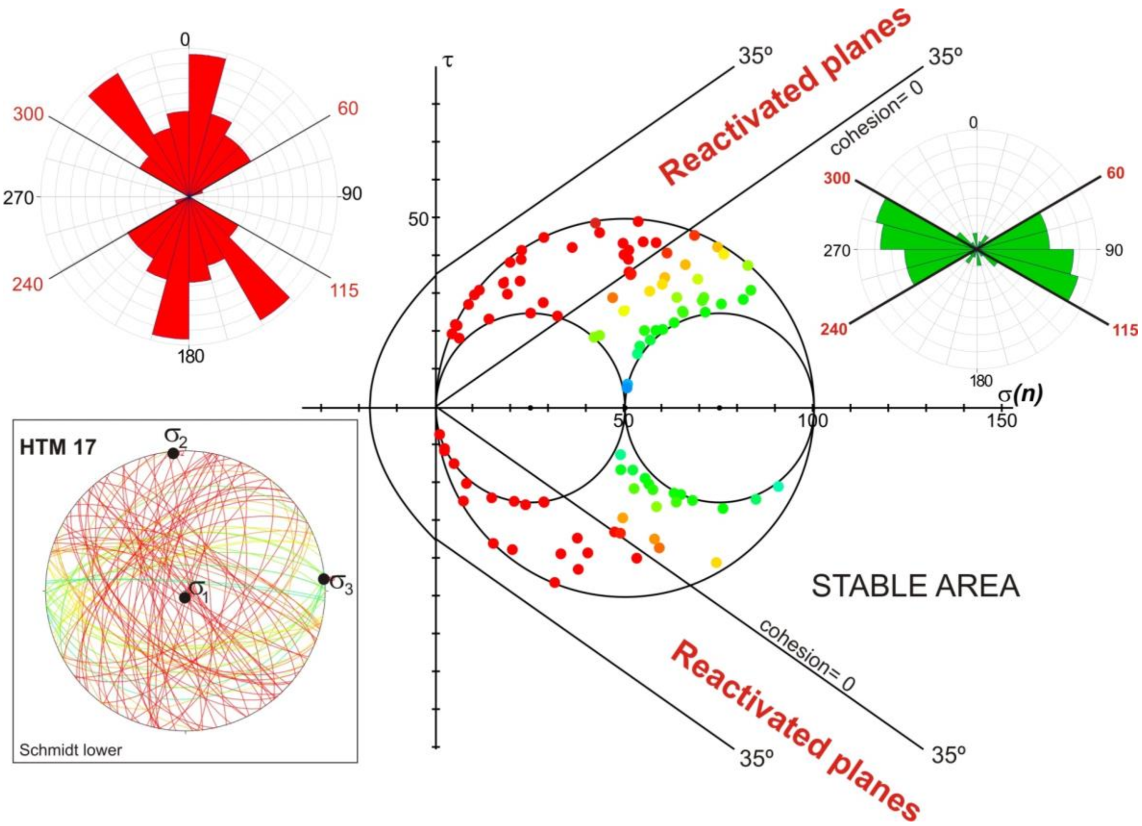

Figure 10. Mohr-Coulomb failure analysis for the fault-slip data measured in HTM17 under the present-day stress tensor determined by Herraiz et al. (2000). Red dots are faults reactivated, and green and orange dots are located within the stable zone. Red rose diagram shows the orientation of reactivated faults, between N-S to N60ºE and from N115ºE to N180ºE. Green rose diagram shows the fault orientation for faults non-reactivated under the active tress field within the area. See text for further details. The yellow data in the M-C diagrams are referred to those planes close to be reactivated, and potentially reactivated by increasing the pore pressure.

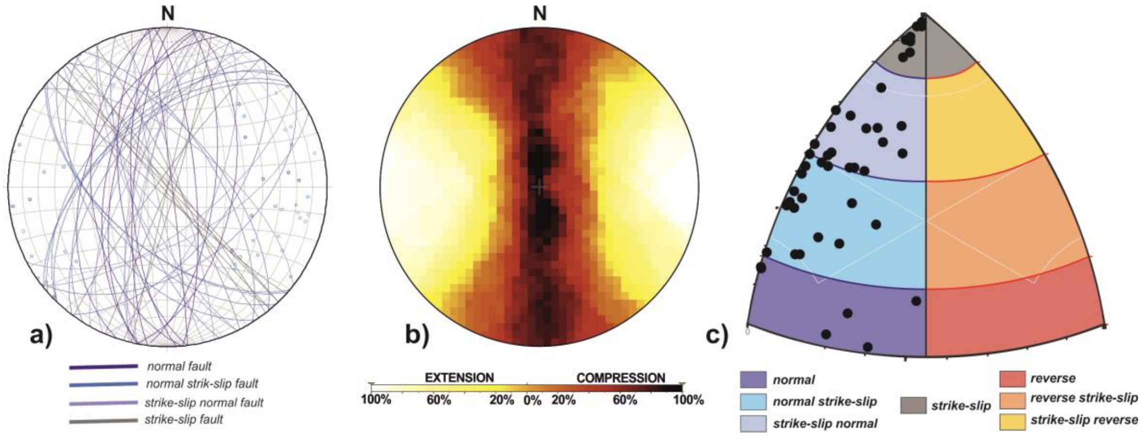

Figure 11. a) Stereogram and poles of fault sets (HTM17) reactivated under the present-day stress field suggested by Herraiz et al. (2000). b) Right-Dihedral of the reactivated fault sets. c) K'-strain diagram showing the type of fault for each fault-set.

TABLE CAPTIONS

K'	*T-axis*	*strain axis rel.*	*fault type*	*tectonic field*
< - 0.5	0º	$e_z > -e_x = -e_y$	normal	pure radial extension
-0.5<K'<0	0º-45º	$e_z > -e_x > -e_y$	normal	radial extension
K'=0	0º-45º	$e_z = -e_x;\ e_y = 0$	normal	plain strain
0<K'<1	0º-45º	$-e_x > e_z > e_y$	normal with SS	extension with shear
k=1	0º-45º	$-e_x > e_y = e_z$	normal with SS	extension with shear
1<K'<10	0º-45º	$-e_x > e_y > e_z$	strike-slip with N	shear with extensional
10<K'<∞	0º-45º	------------	strike-slip	shear deformation
K'=∞	45º	$e_z = 0; -e_x = e_y$	strike-slip	pure shear deformation
∞<K'<-11	45º-90º	------------	strike-slip	shear deformation
-11<K'<-2	45º-90º	$e_y > -e_x > -e_z$	strike-slip with R	shear with compression
K'=-2	45º-90º	$e_y > -e_x = -e_z$	reverse with SS	compression with shear
-2<K'<-1	45º-90º	$e_y > -e_z > -e_x$	reverse with SS	compression with shear
K'=-1	45º-90º	$-e_z = e_y;\ e_x = 0$	reverse	plain strain
-1<K'<-0.5	45º-90º	$-e_z > e_y > e_x$	reverse	radial compression
K'=-0.5	45º-90º	$-e_z > e_y = e_x$	reverse	pure radial compression

SS = strike-slip — e_x = value of the minimum horizontal shortening
N= normal — e_y = value of the maximum horizontal shortening
R= reverse — e_z = value of the vertical axis

Table 1. Different tectonic regimes, K' values, dip values and fault type for the Kaverina modified diagram used in this work. According to the strain axes relationship, faults can be classified and the tectonic regime can be established.

STATION	nº faults	series/epoch	Dey (°)	dispersion	strain tensor
HTM11	8	MIDDLE MIOCENE	50	4	NORMAL STRIKE-SLIP
HTM30	6	EARLY-MIDDLE MIOCENE	145	21	COMPRESSION
HTM15	13	EARLY-MIDDLE MIOCENE	33	25	COMPRESSION
HTM10	8	EARLY-MIDDLE MIOCENE	69	13	NORMAL STRIKE-SLIP
HTM01	7	EARLY-MIDDLE MIOCENE	70	22	NORMAL STRIKE-SLIP
HTM13	24	EARLY OLIGOCENE	25-160	23	NORMAL STRIKE-SLIP
HTM32	6	UPPER CRETACEOUS	90	7	NORMAL
HTM31	11	UPPER CRETACEOUS	108	16	STRIKE-SLIP NORMAL
HTM29	8	UPPER CRETACEOUS	179	24	STRIKE-SLIP NORMAL
HTM26	10	UPPER CRETACEOUS	0	23	STRIKE-SLIP
HTM25	11	UPPER CRETACEOUS	141	26	STRIKE-SLIP COMPRESSION
HTM23	14	UPPER CRETACEOUS	99	15	STRIKE-SLIP
HTM22	5	UPPER CRETACEOUS	175	8	NORMAL STRIKE-SLIP
HTM21	14	UPPER CRETACEOUS	138	22	STRIKE-SLIP NORMAL
HTM20	11	UPPER CRETACEOUS	75	5	STRIKE-SLIP
HTM19	20	UPPER CRETACEOUS	61	30	NORMAL STRIKE-SLIP
HTM17	105	UPPER CRETACEOUS	107	24	NORMAL
HTM08	10	UPPER CRETACEOUS	45	11	STRIKE-SLIP
HTM3	8	UPPER CRETACEOUS	25	6	STRIKE-SLIP (N-C)
HTM2	34	UPPER CRETACEOUS	150	18	STRIKE-SLIP (N-C)
HTM14	8	LOWER CRETACEOUS	34	21	COMPRESSION
HTM5	18	UPPER TRIASSIC	140	8	NORMAL STRIKE-SLIP

Table 2. Summary of the outcrops showing the number of faults, the type of the strain tensor obtained, the Dey, S_{Hmax} striking and the age of the affected geological materials. N-C is normal component for strike-slip movement.